DIPLOMARBEIT

Monte Carlo simulated model of a preclinical PET insert and experimental validation based on NEMA performance measurements

ausgeführt am Atominstitut (E 141)
der Technischen Universität Wien

in Zusammenarbeit mit dem

Zentrum für Medizinische Physik und Biomedizinische Technik
der Medizinischen Universität Wien

unter der Anleitung von

Ass.Prof. Dipl.-Ing. Dr.techn. Albert Hirtl
(Technische Universität Wien)

und

Dipl.-Ing. Ivo Rausch, PhD
(Medizinische Universität Wien)

durch

Nicole Jurjew
Matr.-Nr.: 01026753

Ort, Datum

Prof. A. Hirtl

Acknowledgements

First and foremost, my thanks go to Ivo Rausch, who answered all my questions with great patience. He gave me not only the opportunity to learn about molecular imaging, but was also an endless source of hunting and fishing stories.

Further, I would like to thank Albert Hirtl, whose lecture introduced me to functional imaging in the first place and whose precision helped me to improve my scientific work.

My sincerest gratitude goes to Hunor Kertesz, who didn't only have time for constructive feedback whenever asked for, but also for reassuring and calming words whenever needed. Also, thanks to him, I feel much more confident in my role as a Millennial.

Furthermore, I would like to thank Thomas Beyer and the QIMP team, who never treated me as the Greenhorn I was (alright, let's face it, still am), but as one of them, welcoming me to seminars, workshops and, most importantly, discussions about the substantial things in life: Gansl, cookies and dogs.

Of course, I would like to thank my family: My mother, who still believes in me, when I don't and my father, whose critical perception of things is essential in all aspects of life. And, of course, my thanks go to my brother, who would go to the end of the world with me, even in an Opel Corsa, provided there's a parking garage.

Thank you to my friends Juliana and Magdalena, who gave me countless pep talks and discussed "the Afterlife" to much extent, even being distributed all over the world.

And to my dear "Spritzweinbande", who discussed cross sectional values, LaTeX-bugs and flowerpots with me, in the middle of night, day and a pandemic.

Affidavit

I, Nicole Jurjew, hereby declare in lieu of oath, that I performed all work for this project myself and that I executed all associated research on my own. For writing this thesis, I only used literature cited in this volume and if text passages from those sources are used literally, they are marked as such.
I confirm that this work is original and has not been submitted elsewhere for any examination, nor is it currently under consideration for a thesis elsewhere.

Place, Date

Abstract

Positron Emission Tomography combined with Magnetic Resonance (PET/MR) is a medical imaging method, used to investigate the distribution of a previously administered radioactive tracer in humans or animals. Among others, it can be used for diagnosis of cancer and neurological disorders. Before newly developed methods or tracers can be used in clinical routines, extensive research is necessary. This can be done using preclinical scanners, specifically designed for imaging small animals such as mice or rats, or using Monte Carlo simulations to reproduce the imaging process. However, Monte Carlo (MC) models for available scanners need to be established and compared to the real systems.

In this work, a preclinical PET/MR system, the model "Si 198", manufactured by the "Bruker BioSpin GmbH", available at the Medical University of Vienna, was experimentally characterized following standardized performance measurements. Subsequently, the system was modeled in the MC simulation environment GATE. Then, the performance of the MC model was compared to its real counterpart.

Specifically, the performance of the system was determined following the standardized measurement protocol "NEMA NU4-2008". In this process, the scanner was assessed regarding its sensitivity to radioactivity, its count rate behavior, its spatial resolution and the resulting image quality. For sensitivity measurements, a ^{22}Na point source was stepped through the field of view along the scanner axis and the count rate was brought in relation to source-activity. To evaluate the count rate behavior, two ^{18}F line sources in polyethylene - cylinders with different dimensions were measured and the acquired counts were classified in scattered, random and true counts. The measurements for spatial resolution evaluation were performed with the same point source as sensitivity measurements, whereas for spatial resolution, the source was stepped transaxially through the field of view. The image quality was assessed using a complex cylinder system made from PMMA, which was filled with

an aqueous solution of ^{18}F.

The main focus of this thesis was, however, the creation and validation of a copy of the scanner, generated with the Monte Carlo simulation software GATE. Subsequently, all measurements described before were also simulated and the results were compared to the actual measurements.

Performance parameters measured for the preclinical system were in accordance with published parameters of similar systems. However, parameters calculated for the MC model were only partly in agreement with the measured data. For example, the count rate performance parameters found in the MC model were strongly affected by the parameter settings in the MC code. Real measurements could partially be reproduced, however, no generally applicable parameter configuration could be found so that the model realistically mimics the observed scanner.

In summary, the performance parameters of the Bruker PET insert could be experimentally assessed. It was possible to establish an MC model of the system. Nevertheless, for a general applicability of the MC model, an optimization of the parameter set would be required. However, this optimization seems only feasible with the availability of specific information about the system electronics from the vendor.

Kurzfassung

PET/MR ist ein bildgebendes Verfahren, bei dem die Verteilung eines zuvor injizierten radioaktiven Tracers in Menschen oder Tieren untersucht wird. Diese Methode wird zum Beispiel zur Diagnose von Krebs oder neurologischen Erkrankungen eingesetzt. Bevor neu entwickelte Verfahren oder Tracer im klinischen Umfeld angewendet werden können, ist umfangreiche Forschungsarbeit notwendig. Diese kann an präklinischen Scannern, die eigens für die Bildgebung kleiner Säugetiere wie Mäusen oder Ratten entwickelt wurden, oder durch die Verwendung von Monte Carlo Simulationen, mit Hilfe derer der Bildgebungsprozess reproduziert werden kann, durchgeführt werden.

In der vorliegenden Arbeit wurde ein präklinisches PET/MR System, das Modell "Si 198", hergestellt von der "Bruker BioSpin GmbH", welches auf der Medizinischen Universität Wien verfügbar ist, experimentell charakterisiert. Dabei wurde einem standardisierten Performance Messprotokoll gefolgt. Danach wurde das System in der MC Simulations Umgebung GATE modelliert. Anschließed wurde die Leistung des MC Modells mit jener seines tatsächlich existierenden Gegenstücks verglichen.

Konkret wurde die Performance des Systems mit Hilfe des standardisierten Messprotokolls "NEMA NU4-2008" bestimmt. In diesem Prozess wurde der Scanner hinsichtlich seiner Empfindlichkeit gegenüber Radioaktivität, seines Zählratenverhaltens, seiner Ortsauflösung und der resultierenden Bildqualität untersucht. Für die Empfindlichkeitsmessungen wurde eine ^{22}Na Punktquelle entlang der Scannerachse durch den Sichtbereich bewegt und die Zählrate in Verhältnis zur Aktivität gebracht. Um das Zählratenverhalten zu beurteilen, wurden zwei ^{18}F Linienquellen in Polyethylen Zylindern mit unterschiedlichen Dimensionen gemessen und die erfassten Counts in Streu-, Zufalls- und "echte" Counts klassifiziert. Die Messungen zur Beurteilung der Ortsauflösung wurden mit der selben Punktquelle durchgeführt, wie die Empfindlichkeitsmessungen, wobei die Quelle hierfür transaxial durch den

Scanner bewegt wurde. Die Bildqualität wurde mit einem komplexen Zylinder-System aus Plexiglas, welches mit einer ^{18}F Lösung gefüllt wurde, gemessen.

Das Hauptaugenmerk der vorliegenden Arbeit sollte jedoch die Erstellung und Validierung eines Modells ebenjenes Scanners mit der Monte Carlo-Simulationssoftware GATE sein. Darauffolgend wurden alle zuvor beschriebenen Messungen simuliert und deren Ergebnisse wurden mit jenen der tatsächlich durchgeführten Messungen verglichen.

Die Performance Parameter, die für das präklinische System gemessen wurden, stimmten mit veröffentlichten Werten ähnlicher Systeme überein. Die Parameter, die für das MC Modelle gemessen wurden, waren nur teilweise mit den gemessenen Resultaten kongruent. Zum Beispiel wurden die Zählraten Parameter, die für das MC Modell bestimmt wurden, stark von den Parameter Einstellungen im MC Code beeinflusst. Die tatsächlichen Messungen konnten teilweise reproduziert werden, es konnte jedoch keine allgemein anwendbare Parameterkonfiguration gefunden werden, so dass das Modell den untersuchten Scanner bei jeder Messung realistisch imitierte.

Zusammenfassend kann gesagt werden, dass die Leistungsparameter des Bruker PET Inserts experimentell bestimmt werden konnten. Ein MC Modell des Systems wurde erfolgreich kreiert. Nichtsdestotrotz wäre für eine allgemeine Anwendung des MC Modells eine Optimierung des Parameter Sets notwendig. Diese Optimierung scheint allerdings nur mit dem Zugang zu spezifischer Scanner Information des Anbieters umsetzbar.

Contents

List of figures

List of tables

1. Introduction

Positron Emission Tomography (PET) is a widely used noninvasive method to assess functional processes in vivo. Among others, this means, that cells which have a higher uptake of specific substances relative to their surrounding tissue can be made visible. That way, for example tumor tissue can be identified. However, the functional information only contains limited information about anatomy. This lack of anatomical knowledge gained with PET drove the development of its application together with computed tomography (CT), which was introduced in 2000 [1]. The demand for a combination of PET with magnetic resonance imaging (MRI or MR) becomes evident, considering that MR shows higher soft tissue contrast than CT and, due to the lack of ionizing radiation, implies lower patient dose. The presence of a high magnetic field utilized in MR, however, caused its technical difficulties in development of a combined scanner. For instance, due to the deflection of electric charge in magnetic fields, the light amplification used up to this point (Photo Multiplier Tubes or PMTs) was not suitable. After those issues could be resolved, combined PET/MR systems were introduced [2].

The continuous development of detector technologies, pharmaceuticals and methods reveals more and more fields of application of PET/MR. The use of newly developed methods in humans, however, needs a profound base of preclinical investigations. PET studies of animals, such as nonhuman primates, mice and rats, include development of new pharmaceuticals or PET tracers. Furthermore, newly developed treatment strategies can be tested and courses of disease can be studied [3]. For those applications, follow-up scans of the same animal are indispensable. The noninvasive nature of PET allows for the possibility to investigate the same specimen multiple times, which does not only enable repetitive exams but is additionally economically desirable [4].

Aside from preclinical studies, also scanner simulations provide a useful tool to plan and test PET experiments before development. In simulated image data acquisitions, the flexible adaption of parameters such as crystal size or administered dose enables to investigate their direct influence on image quality. Furthermore, the ground truth for evaluating image reconstruction algorithms is known. GATE is a Monte Carlo simulation software that can be used to simulate emission tomography (ET) [5]. It adds a layer of timing and movement on top of GEANT4 [6], a simulation software by itself, created to simulate particles in high energy physics. There is a vast number of applications of simulated emission tomography data, reaching from scanner design development [7, 8] over dosimetry estimation in nuclear medicine [9] to producing the ground truth for image quality assessment. More and more commercial systems have been simulated and validated [10, 11]. Furthermore, phantoms used in simulations to model imaging situations become more and more realistic. So called voxelized phantoms, which are based on segmented computed tomography (CT) or MR scans, provide very authentic patient-models. This doesn't only mean more detail in anatomy: For example, also a beating heart model [12] and a model for the breathing motion were established [13].

In order to ensure sufficient quality and reliability of PET studies, it is important to have standardized assessment methods concerning scanner parameters. The organization that provides guidelines to evaluate scanner parameters for various scanner types is called "NEMA", which is short for "National Electrical Manufacturers Association". It is a standard developing organization that "...convenes a neutral forum for Members to discuss industry-wide concerns and objectives under a legal umbrella by trained NEMA staff." [14]. The standard for preclinical PET scanners provides methods to measure spatial resolution, sensitivity, scatter behavior and image quality [15].

The aim of this work was to create and validate a Monte Carlo simulated model of a preclinical PET insert available at the Preclinical Imaging Laboratory (PIL) at the Medical University of Vienna. The insert, model "Si 198" [16] was manufactured by Bruker BioSpin GmbH and it is placed inside a 9.4 T MR at PIL. For validation, the measurements described in the NEMA standard *NEMA NU 4 - 2008 Performance Measurements of Small Animal Positron Emission Tomographs* [15] for sensitivity, spatial resolution, scatter behavior and image quality were performed and analyzed. Then, the open source software GATE was used to create a model of the scanner. All NEMA measurements were also carried out on the simulated scanner and results were compared.

2. Technical Background

In this chapter, a basic explanation of PET Imaging and GATE simulations are given. Descriptions are mainly based on [4, 17, 18].

2.1 PET - Signal Formation

In PET, ionizing radiation produced by radioactive decay is used to observe the processes of interest in the human body. In particular, radionuclides decaying via the β^+ branch are used for PET imaging (see section 2.1.1 for more details). To utilize β^+ emitters for PET imaging, they are bound to biological molecules which accumulate in specific tissue or organs, thus forming a radiopharmaceutical called "tracer". The use of radioisotopes to track a dynamic process in an organism was discovered and studied by George de Hevesy in 1923, who also phrased the "Tracer principle" [19]: Adding small amounts of a radioactively labeled biomolecule to the body doesn't influence the physiologically present molecules. If, however, too much substance is added, this doesn't apply anymore. As the key is to only use very small amounts, the substance gained its name "tracer". With PET, the tracer-distribution can be measured non-invasively and in doing so, functional processes can be visualized.

2.1.1 Beta - Decay and Positron Annihilation

Radioactive decay occurs when the excited nucleus of an atom emits its excess energy to return into a stable state. This can in principal happen via α, β^+ or β^- or γ emission. During β^+ decay, a proton p converts into a neutron n, a positron e^+ and an electron-neutrino ν_e. Due to the transformation of a proton into a neutron, the mother nucleus is another chemical element than the daughter nucleus, while their mass numbers are the same.

$$\mathrm{p} \longrightarrow \mathrm{n} + e^{+} + \nu_e$$

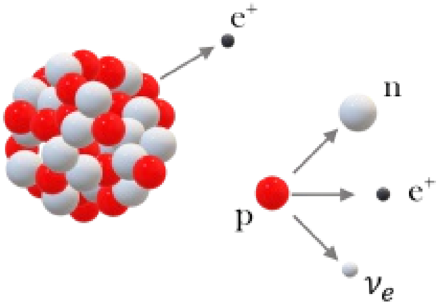

Figure 2.1: As a result of a nucleus undergoing β^{+} decay (left), a proton converts into a neutron, a positron and an electron neutrino (right).

As stated before, β^{+} emitters decay under emission of positrons. Positrons and electrons are antiparticles, meaning they have (amongst others) the same mass and spin, but the opposite electric charge. Therefore, they interact with each other upon collision. To be more specific, electrons and positrons can annihilate and their energy causes the creation of two photons. Conservation of momentum urges the photons to be emitted with ≈180 ° between them, while due to energy-conservation they have the same energy as positron and electron, namely 511 keV each. An illustration of β^{+} decay can be found in figure 2.2. Depending on the isotope, positrons can have kinetic energy after ejection, which causes them to travel through matter before interacting with an electron. The distance they are traveling also depends on the material in which the emission happens and is called positron range.

2.1.2 Interactions of Photons with Matter

There are many different types of photon interaction with matter which can be classified according to their location of interaction: The atomic shell, the atomic nucleus or the Coulomb field surrounding the atomic nucleus. Which effect occurs strongly depends on the photon's energy. Thus, only the most relevant effects applying to the 511 keV photons in PET are listed and explained below.

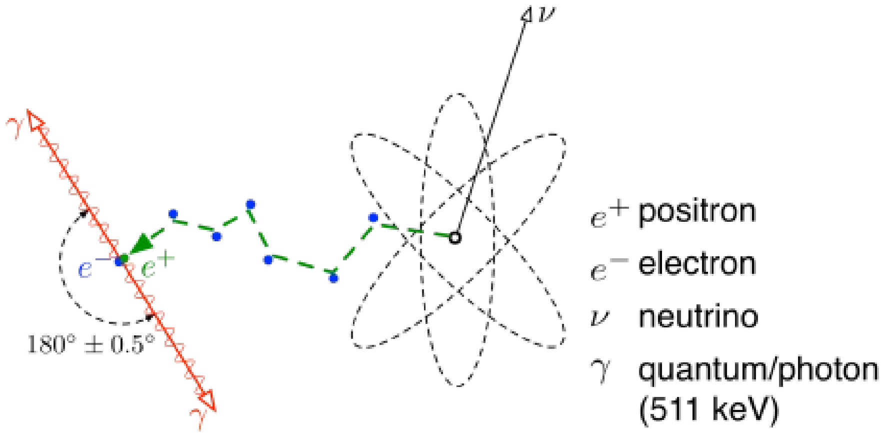

Figure 2.2: Positron Annihilation: Following beta decay, a positron is ejected from the nucleus (right) and travels through matter (dashed line) before interacting with an electron. Upon annihilation, two gamma quants are emitted at an angle of ≈180 °. Source: [20]

Compton Scattering Compton scattering denotes the interaction of an incident photon with an outer shell electron that is loosely bound. A visualization can be found in figure 2.3 a. The incident photon's energy is much higher than the electron's binding energy, hence only part of the photon's energy is transferred to the electron. As it loses energy, the photon is deflected from its initial trajectory and its wavelength is increased. The angle θ, with which the photon is scattered only depends on the photon's energy loss. The scattered photon's energy E_{sc}, its initial energy E_γ and the scattering angle θ are connected via

$$E_{\mathrm{sc}} = \frac{E_\gamma}{1 + \frac{E_\gamma}{511}(1 - \cos\theta)}. \tag{2.1}$$

The numerical value 511 has the unit keV as it is the electron's rest mass. The angular distribution of Compton scattered photons is given via the so called "Klein-Nishina" equation:

$$\frac{\mathrm{d}\sigma}{\mathrm{d}\Omega} = Zr_e^2 \left(\frac{1}{1 + \beta\,(1 - \cos\theta)}\right)^2 \left(\frac{1 + \cos^2\theta}{2}\right) \left(1 + \frac{\beta^2(1 - \cos\theta)^2}{(1 + \cos^2\theta)\,(1 + \beta\,[1 - \cos\theta])}\right), \tag{2.2}$$

where r_e is the classical radius of the electron, Z is the atomic number of the scattering material and the ratio of photon energy E_γ to electron rest mass energy $m_e c^2$ is called $\beta = E_\gamma / m_e c^2$. The general probability σ_C of Compton scattering occurring upon interaction of a photon and an electron is calculated by integrating equation (2.2) over all possible solid angles, which leads to

$$\sigma_C = 2\pi r_e^2 \left\{ \frac{1+\beta}{\beta^2} \left[\frac{2\,(1+\beta)}{a+2\beta} - \frac{1}{\beta} \ln(1+2\beta) \right] + \frac{1}{2\beta} \ln(1+2\beta) - \frac{1+3\beta}{(1+2\beta)^2} \right\}. \tag{2.3}$$

The Photoelectric Effect ”Photoelectric effect” denotes a type of photon interaction with the atomic shell, where the photon’s energy is fully absorbed by an inner shell electron of the atom, depicted in figure 2.3 b. Within this process, the photon’s energy is transferred to the kinetic energy of respective electron, causing it to be emitted. This event is called photoionization and for incident photon energies less than the rest mass energy of the electron but greater than the K-shell electron binding energy, the probability σ_p for it to happen is given by

$$\sigma_p = \frac{32}{3} \sqrt{2} \pi r_e^2 \alpha^4 Z^5 \left(\frac{m_e c^2}{E_\gamma} \right)^{7/2}. \tag{2.4}$$

In equation (2.4), α is the fine structure constant, Z is the atomic number, r_e and m_e are the electron’s classical radius and its rest mass energy, respectively and E_γ is the incident photon’s energy. Equation 2.4 has to be multiplied by a factor proportional to $(1/Z^2)(m_e c^2/E_\gamma)^{1/2}$ if the incident photon’s energy is in the order of K-, L- or M-shell binding energies and if the incident photon’s energy is greater than the electron’s rest mass, relativistic effects require equation (2.4) to be multiplied with a factor proportional to $(m_e c^2/E_\gamma)^{3/2}$.

2.1.3 Radiation Detection

There are multiple possibilities to detect ionizing radiation in PET. When the first scanners were developed, so called proportional gas chambers had been in use in high

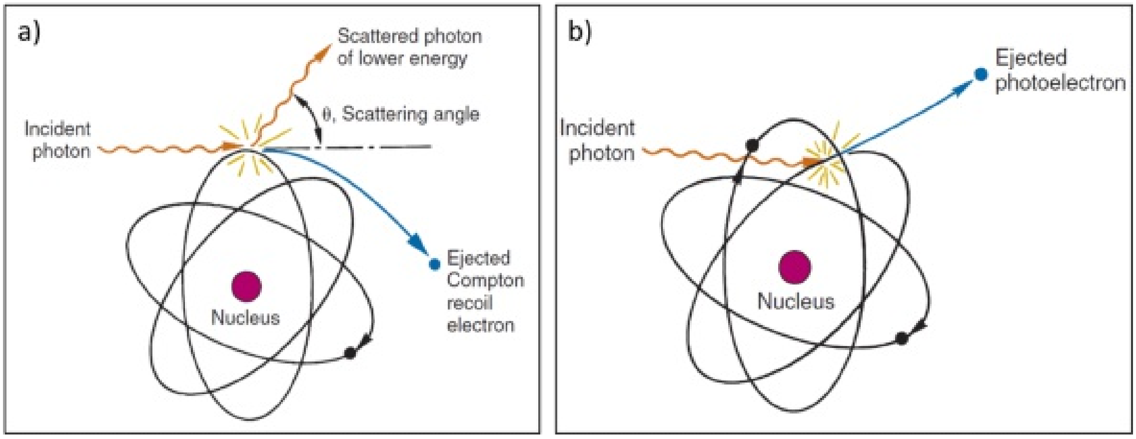

Figure 2.3: (a) Compton scattering occurrs, when a photon interacts with a loosely bound electron of an atom. The photon is deflected from its original trajectory and loses energy. (b) The photoelectric effect occurrs, when an incident photon interacts with the inner shell electron of an atom. Here, the photon can be absorbed by the atomic nucleus and the electron is ejected. Source: [21]

energy physics for a long time [17] so this technology was the first to be exploited in PET. As proportional gas chambers have poor energy resolution and stopping power for 511 keV photons, however, other types of radiation detectors were developed. Currently, the most commonly used radiation detectors utilized in PET are based on scintillator crystals, their main alternative being semiconductor detectors [18].

While semiconductor detectors show excellent energy resolution, their stopping power is relatively poor for 511 keV photons and they are more costly than scintillator crystals. Their functioning principle is based on semiconductors' typical band structure. Ionizing radiation lifts electrons from the valence band to the conductance band and electron hole pairs are created. The resulting charge is proportional to the incident photon's energy and can be collected by applying an electric field. The application of semiconductor detectors allows for the direct conversion of incident radiation to an electric signal.

Despite their poor energy resolution, scintillation detectors show the best stopping power, which explains why they are utilized most commonly in PET scanners. Inorganic crystals are primarily used as PET-scintillation detectors. A crystal atoms' shell electron is lifted to an excited state when a high energy photon transfers its energy to it. The excess energy is then released via emission of a photon when the electron returns to its stable state. For most scintillation detectors, the emitted photon would be in the ultraviolet range. To achieve emission of visible light, scintillator crystals are doped with impurities (e.g. Thallium to NaI).

Inorganic crystal compositions utilized in PET are BGO (bismuth germanium oxide, $Bi_4Ge_3O_{12}$), LSO (lutetium oxyorthosilicate, Lu_2SiO_5) and LYSO (lutetium yttrium orthosilicate, $Lu_{2-x}Y_xSiO$), amongst others. The scanner examined within this work uses LYSO, which contains Lutetium. Around 3 % [22] of naturally occurring Lutetium is present as a radioactive isotope, ^{176}Lu, which decays via β^--radiation. This ionizing radiation interacts with the detector material, leading to counts being detected by the scanner which origin from the detector material rather than from the source within the FOV. This count rate, which is called intrinsic or background count rate, can be measured by a so called background scan: Counts are acquired with the scanner without any source being present in the FOV during measurements.

To achieve the conversion of visible light into an electric signal, photomultiplier tubes (PMTs) are most commonly used, which serve well to explain the basic principle of light amplification. An illustration of a photomultiplier tube is given in figure 2.4. In PMTs, a photon causes a photoelectron to leave the photo-cathode which is subsequently accelerated towards a dynode where it knocks out multiple additional electrons. This process is repeated by applying and electric field, until all electrons reach the anode. The resulting current is proportional to the energy of the incident photon.

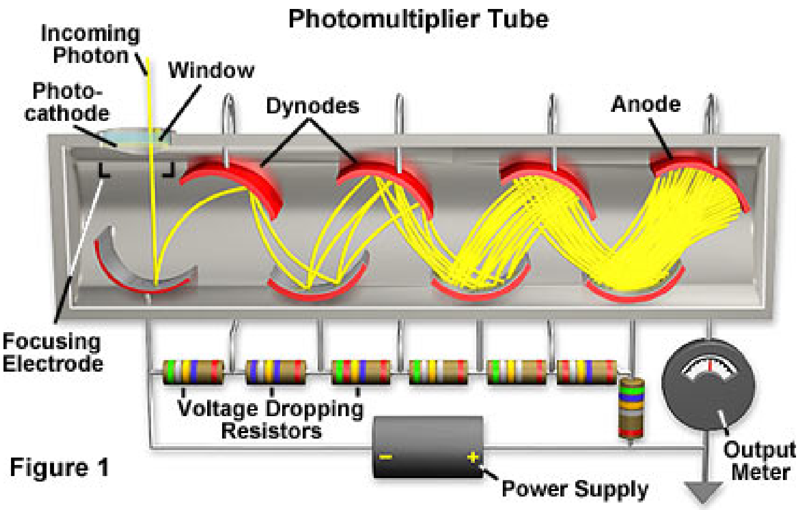

Figure 2.4: Sectional illustration of a photomultiplier tube. The incident photon causes an electron to be ejected from the photo cathode. The electron is then accelerated to a dynode, where it causes multiple electrons to be ejected. This process is repeated multiple times, hence transforming the incident photon's energy to an electrical signal. (Source: [23])

PMTs can't be used in MR because electrical charge is deviated in magnetic fields. This called for the use of semiconductor detectors insensitive to magnetic fields, such as avalanche photo diodes (APDs), to convert visible light emerging from the scintillation process into an electric signal. As is illustrated in figure 2.5, in APDs layers of varying constitution with different purposes are utilized to accomplish this transformation. In the absorption layer, visible light quants are converted into an electron hole pair. Due to the external voltage applied, electrons are then accelerated in accordance with the electric field. In the multiplication area, because of the different constitution of the semiconductor material, the electric field is stronger, causing further electron-hole pairs to be created. The electron avalanche that is created this way is proportional to the initial amount of electron-hole pairs and thus the incident photon's energy. APDs have a low signal gain (10^2 compared to 10^5 - 10^6 for PMTs [18]) and also the time between an incident photon hitting the detector and a rise in the electrical output signal (signal rise time) is longer [4].

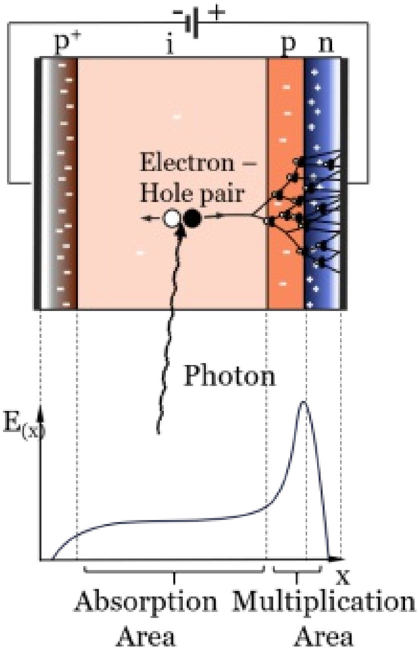

Figure 2.5: Illustration of the layers and the resulting electric field of an avalanche photo diode (APD). An incident photon creates an electron hole pair in the absorption area, which is then accelerated towards the multiplication area. There, the charge carrier causes an avalanche of further electrons to be ejected. With courtesy of Ivo Rausch.

So called silicon photomultipliers (SiPMs) were developed which overcome both of those issues (see figure 2.6 for an example). SiPMs are arrays of densely packed

APDs which are run in Geiger-mode, meaning above the breakdown voltage. The APDs are operated in parallel [24], which means that SiPMs can detect more photons at the same time. Overall, SiPMs have a higher gain than APDs, similar to PMTs (10^5 - 10^6 for SiPMs compared to 10^2 for APDs [18]) and their timing resolution is in the order of several tens of ps [24], making SiPMs sutiable for a PET operation mode called "time of flight" (TOF). In this mode, the timing difference between two annihilation photons hitting opposite detectors can be measured, which makes the estimation of the annihilation point during image reconstruction more precise. As APDs have slower input response in the order of ns [18], they are not applicable for TOF-PET.

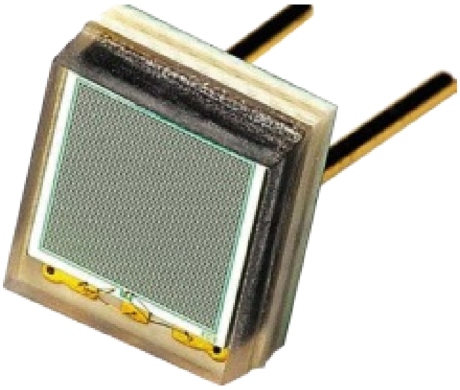

Figure 2.6: Picture of a Silicon Photomultiplier, consisting of an array of Avalanche Photo Diodes. (Source: [25])

2.1.4 Coincidence Counting

To visualize the tracer distribution within an object under investigation, the scanner software needs to determine if two individually detected photons (Singles) can be assigned to the same annihilation process. This is done by coincidence detection. As annihilation photons are produced at the same time, simultaneously measured photons are regarded as originating from the same annihilation process. Because the photons don't necessarily travel through the same distances and materials, however, they most likely arrive with a time shift. This leads to the application of a coincidence timing window, meaning that singles being detected up to a maximum time span are still regarded as simultaneous.

To receive an estimation for the order of magnitude of the coincidence timing window, two photons that were emitted right in front of a detector surface can be taken into consideration. While traveling with the same velocity ($3 \times 10^8\,\mathrm{m\,s^{-1}}$), the photons have to cover different distances before being detected by the scanner. For simplification, the maximum detector distance can be assumed as 1 m, resulting in a timing difference of $t = \frac{1}{3\cdot 10^8} s = 3.3\,\mathrm{ns}$ via $v = \frac{s}{t}$. Thus, taking the scanner geometry into account, a lower threshold for the coincidence timing window is obtained. An upper threshold is selected to reduce detection of random events (more details in chapter 2.2).

For each coincidence, the line connecting the corresponding single events is called line-of-response (LOR). This means, that the positron annihilation detected originated somewhere on the LOR. Hence, the summed signal along a LOR corresponds to a projection of the activity distribution along respective LOR. Section 2.1.1 explains, why annihilation photons have to be emitted with ≈180 ° between them. By applying an acceptance angle above which coincidences are dismissed as they are likely to originate from scattered events, falsely detected coincidences (see chapter 2.2) can be limited. More specifically, only events for which the annihilation photons were measured by detectors which are connected by a LOR within a pre-defined acceptance angle in the transaxial plane are considered as true. An illustration can be found in the left of figure 2.7.

Furthermore, the ring distance for coincidences can be restricted. This means that for a given ring m, only coincidences formed together with detectors of a ring within a certain distance z are considered as true events. The illustration in figure 2.7 shows this scenario.

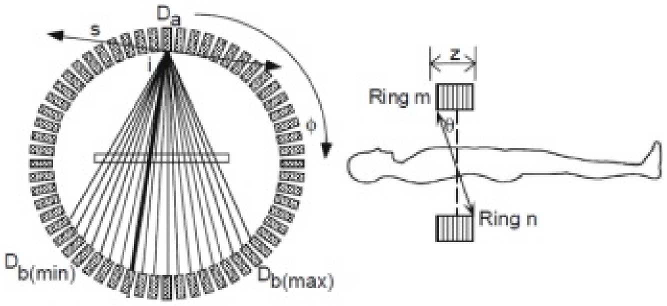

Figure 2.7: Acceptance angle and ring difference of a scanner – Left: Detector element $\mathrm{D_a}$ can only produce true events with detectors $\mathrm{D_{b(min)}}$ to $\mathrm{D_{b(max)}}$ within the transaxial acceptance angle. Right: Definition of ring difference z. Source: [17]

By restricting the ring difference for a scan, photons hitting the detector at small angles to the detector surface are avoided. For such interactions, it is difficult to determine the so called depth of interaction (DOI). It denotes the distance between detector surface and interaction point of the photon inside the detector material. Thus, a LOR between the detector surface centers is assumed instead of the true LOR, which leads to a blurred image (figure 2.8). This effect is also called "parallax error"

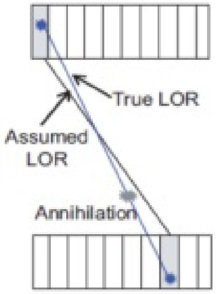

Figure 2.8: Parallax error – In scanners without depth of interaction (DOI) information, images can be blurred as true lines-of-response (LOR) can deviate from assumed LORs. (Source: [26])

2.2 PET - Event Classification

Even with all precautions taken, the scanner software will still detect events that didn't originate from the same positron interaction or where the LOR was altered. To be able to distinguish, all detected events can be divided in "true", "random" and "scattered" events. Coincidences, which truly originate from the same annihilation and where the correct LOR was assigned are denoted as **true**. Coincidences, for which the single events originate from different annihilations are called **random**, while **scattered** events originate from the same annihilation, but one or both photons were deviated before hitting the detector. When three or more events are detected within the coincidence timing window, the coincidence is called **multiple**. As it is impossible to determine which photons originate from the same positron annihilation, such events are usually dismissed. A visualization of the LORs that are detected for all events can be found in figure 2.9.

When a coincidence is detected by a scanner's software, it is not obvious if it is a "true", "random" or "scattered" count. To minimize the contribution of falsely detected counts, however, some precautions can be taken. At high activities, many

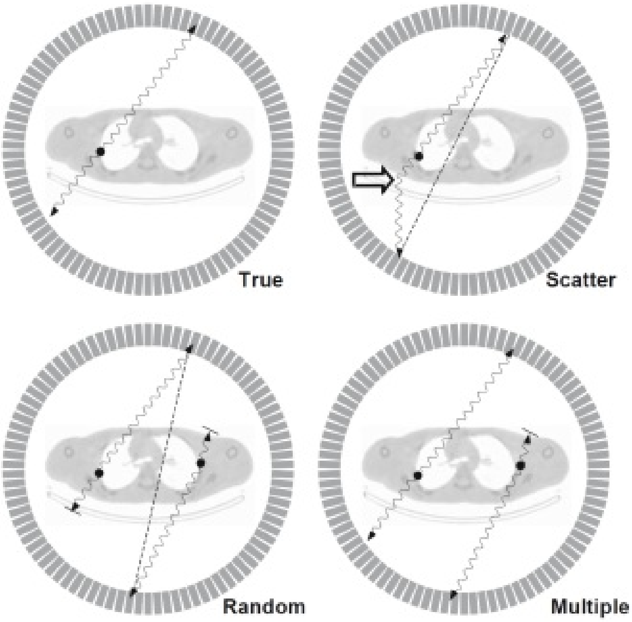

Figure 2.9: Lines of Response for coincidence classification in PET (Source: [17])

decays occur simultaneously, leading to higher random count rates compared to low activities. Nevertheless, after a certain timing window succeeding the detection of a single photon it can be ruled out that a true annihilation partner is found. This can be utilized to estimate for random coincidences by applying a delayed coincidence window and classifying all counts detected within as "randoms". There is another method called "singles method" which can be used to estimate random events. Here, all photon interactions occurring inside a single detector (singles) are logged and then the random coincidence rate on a certain LOR is detected. If i and j are the indices of the detector pair for which a random rate shall be estimated, the random count rate R_{ij} for the LOR connecting them is given by [27]:

$$R_{ij} = 2tr_{\mathrm{i}}r_{\mathrm{j}}, \tag{2.5}$$

where t is the time with which coincidences can be resolved, r_{j} denotes the singles rate measured for detector j and r_{i} is the singles rate measured for detector i respectively. The amount of scatter is linearly related with activity and strongly influenced by tissue properties. As scattered photons have transfered energy to said tissue, they can be limited by tightening the allowed energy window.

2.3 PET - Image Reconstruction

The details described so far don't lead to a three dimensional image of tracer distribution. To provide a basis for understanding image reconstruction and data processing in PET, mathematical descriptions and models are introduced in the following sections.

2.3.1 Analytical Methods

All reconstruction algorithms are based on the mathematical description of the acquired data. For a PET scan, the expectation value of all detected photons is:

$$E\,\{\text{photons detected}\} = \iiint\limits_{VOR} f(\mathbf{x})\, s(\mathbf{x})\, \mathrm{d}\mathbf{x} \tag{2.6}$$

where $f(\mathbf{x})$ denotes the 3-dimensional distribution of activity inside the object under investigation and $s(\mathbf{x})$ is the sensitivity at position $\mathbf{x} = (x, y, z)$. The volume, which connects two relevant detectors is called volume of response (VOR), and is depicted in figure 2.10. In other words, image reconstruction finds a plausible tracer distribution $f(\mathbf{x})$ corresponding to the measured expectation values.

In principle, this is a three dimensional problem and data is acquired this way in state of the art systems. To reduce complexity and thus computational effort, however, 3D-data can be rearranged to form a 2D-problem. To do so, counts from 3D acquisitions, where LORs are not restricted regarding their angle to the scanner axis, are reorganized into two dimensional LOR which are perpendicular to the scanner's main axis. This process is called **single slice rebinning (SSRB)** [28] and is achieved by assigning all counts of a 3D-LOR to that 2D LOR, which intersects the scanner axis at the same axial position. As within this work only SSRB data was used, only two dimensional reconstruction methods are discussed below.

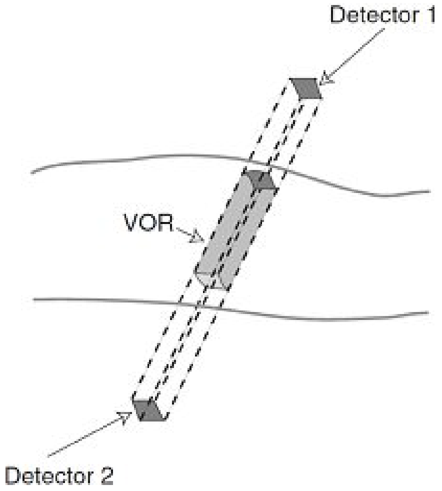

Figure 2.10: A Volume of Response (VOR) is the volume connecting two detector elements. All counts acquired with this detector pair originate from the VOR connecting them (Source: [4])

The data that is obtained for a scan is essentially the number of photons that were measured along a line with a certain angle *phi* and a certain distcance r to the central axis. Inherently, a projection of the object is obtained, which is the line integral along an angle ϕ for all distances x_r within the FOV. This object is also referred to as "Radon transform" and an example is shown in figure 2.11. By gaining the projections for all ϕ, $0 < \phi < \pi$ around an object, a so called sinogram is formed. An example can be found in figure 2.12.

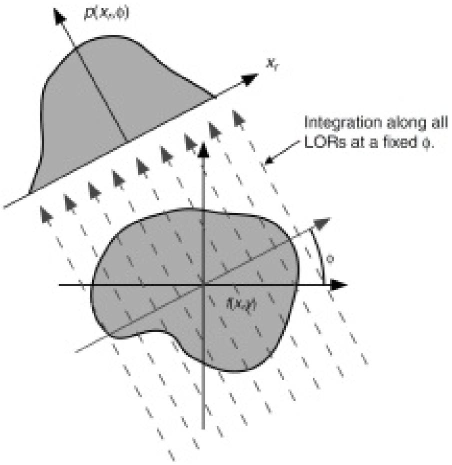

Figure 2.11: Line integration along all LORs for a fixed angle ϕ yields the projection $p(x_{\mathrm{r}}, \phi)$ of an object $f(x, y)$. (Source: [4])

Analytic image reconstruction is based on the **Central Section Theorem**. It

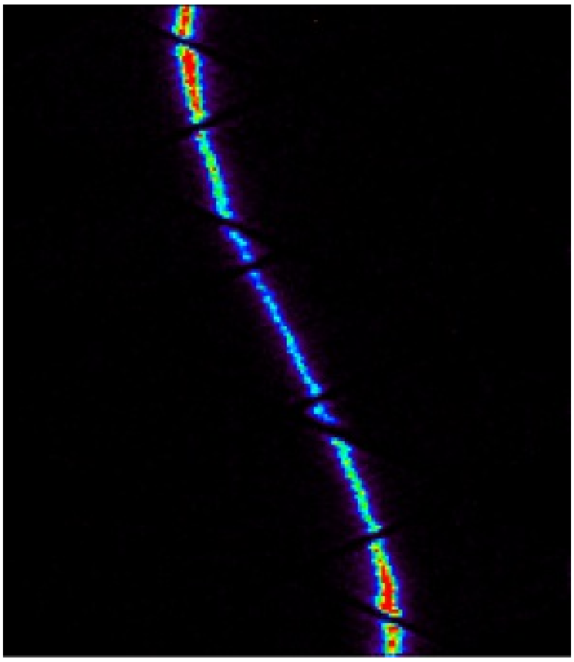

Figure 2.12: Sinogram of a point source scanned with the Bruker PET-insert. the columns of the sinogram represent the distance from center, while the rows correspond with the angle ϕ around the object.

states, that the (inevitably one-dimensional) fourier-transform of a projection for a given angle ϕ is the same as the slice of the two-dimensional fourier transform of the object, which intersects the origin at the same angle ϕ. A visualization is given in figure 2.13. Hence, an image of the object can be obtained knowing the projections for all ϕ, $0 < \phi < \pi$.

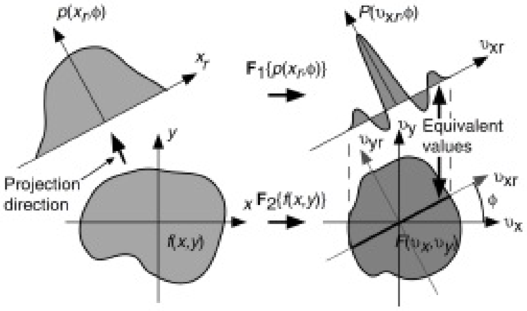

Figure 2.13: Depiction of the two-dimensional central section theorem. The fourier-transform of the projection for an angle ϕ of a two-dimensional object gives the same function as cutting a slice out of the two-dimensional fourier-transform of the original image with the same angle ϕ. (Source: [4])

Backprojection and Filtered Backprojection A simple approach to image reconstruction is called "backprojection". It is carried out by distributing count values received for a certain angle ϕ evenly into all pixels of an image matrix along the same angle ϕ. By repeating this step multiple times, an estimate for the tracer distribution is created. The image obtained is blurred as activity is smeared into pixels where there is none (see figure 2.14 A). A similar attempt is to compute the inverse radon-transform. As hinted above, the radon transform R of a function $f(x,y)$ is the line integral of said function along a line γ which itself is defined by the angle ϕ it takes with the abscissa and the distance r it has to the origin

$$Rf(x,y) = \int_\gamma f(x,y)\,\mathrm{d}x. \tag{2.7}$$

As the parametrization of the line γ can be written as

$$(x(t), y(t)) = (r\cos(\phi) + t\sin(\phi),\, r\sin(\phi) - t\cos(\phi))\,, \tag{2.8}$$

the radon transform of f is

$$Rf(r,\phi) = \int_{-\infty}^{\infty} f\left(r\cos(\phi) + t\sin(\phi),\, r\sin(\phi) - t\cos(\phi)\right)\,\mathrm{d}t \tag{2.9}$$

Forming the radon transform along all lines for a certain angle ϕ, we receive the projection as mentioned in the last chapter. Backprojecting this function into object-space leads to the same result as multiplying the inverse Fourier-transform of the object with the absolute value function of frequencies. As the absolute value-function looks like a ramp, this object is called "ramp filter", but is also referred to as "Ram-Lak" filter and the method itself is called "Filtered Back Projection" (FBP).

2.3.2 Iterative Methods

Analytic reconstruction doesn't reflect the statistical nature of count acquisition and ideal acquisitions are assumed. Iterative reconstructions on the other hand, allow the implementation of mathematical models of physical (attenuation, scatter) or statistical (decay, counting statistics) processes. Their name originates from the repetition of the following steps:

- image estimation
- forward projection into projection space
- comparing estimated with measured projection

If the error is not below a threshold or the desired number of iterations hasn't been reached yet continue:

- project error into image space
- update image guess accordingly
- re-start process

The loop including those steps can be found in figure 2.14 B.

The linear map characterizing the image acquisition model can be written as

$$\mathbf{P} = \mathbf{A}\,\mathbf{f} \tag{2.10}$$

where $\mathbf{P}$ represents the measured projection values, $\mathbf{f}$ denotes the object of the activity distribution and $\mathbf{A}$ is the so called system matrix. It characterizes the system's reaction to decay with regard to its geometry. This model at hand, image-reconstruction essentially translates to estimating the vector $\mathbf{f}$.

As opposed to analytical methods, iterative reconstruction algorithms come with the cost of higher computational effort [4]. Hence, iterative algorithms such as MLEM (Maximum Likelihood Expectation Maximization) [29] and its advanced version, OSEM (Ordered Subsets Expectation Maximization) [30] was only implemented clinically after computing power could be enhanced significantly [31]. As they prove as highly beneficial regarding accuracy and flexibility, iterative reconstruction methods are the method of choice for commercial scanner systems.

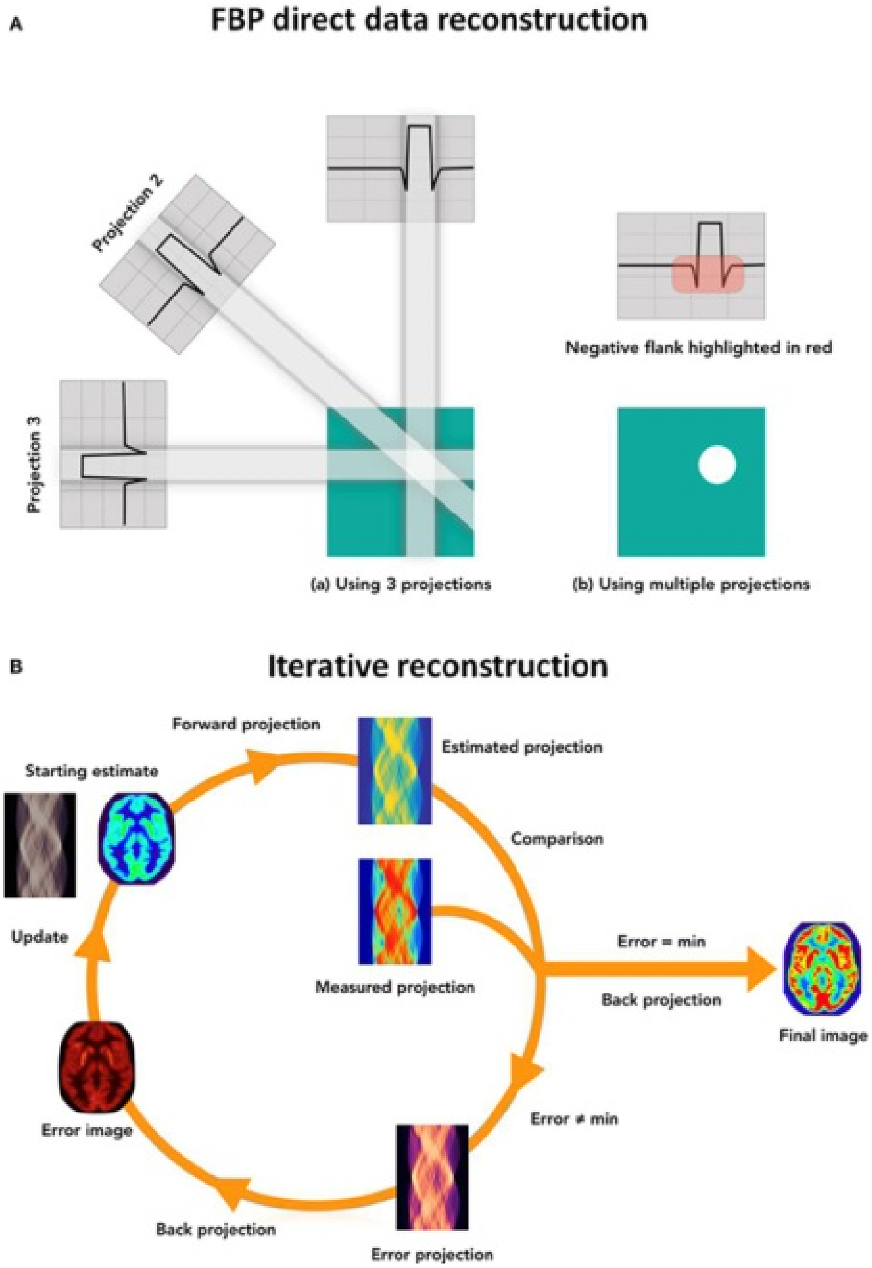

Figure 2.14: Comparison of different reconstruction methods. A) Visualization of the filtered backprojection (FBP) algorithm for different numbers of projections. B) Iteration loop for iterative image reconstruction. (Source: [18])

2.3.3 Data Acquisition in PET

Evidently, a great amount of complex data is acquired in PET imaging. To be able to handle it, some conventions were established for data acquisition.

As explained before, sinograms are a way to save sums of counts along LORs, with each element of the sinogram corresponding to a certain angle ϕ and a certain distance r from the center. In 2D-PET only LORs between opposing detectors are allowed (figure 2.15 A), while in 3D-PET LORs can be restricted but don't have to be perpendicular to the scanner's central axis (figure 2.16 A). So called Michelograms (see figures 2.15 B and 2.16 B) are used to illustrate possible detector pairs in accordance with the allowed acceptance angle and ring difference (see section 2.2). Each cell in a Michelogram that represents an allowed detector-combination is marked with an asterisk. To reduce computation times and also to minimize required storage, data from multiple cells of the Michelogram can be saved cumulatively into a single plane. In this case, those cells are linked in the michelogram. The number of detector pairs that are saved into a single plane is called "span". Figure 2.16 B) shows the michelogram of a 16 ring scanner utilizing a span of 7.

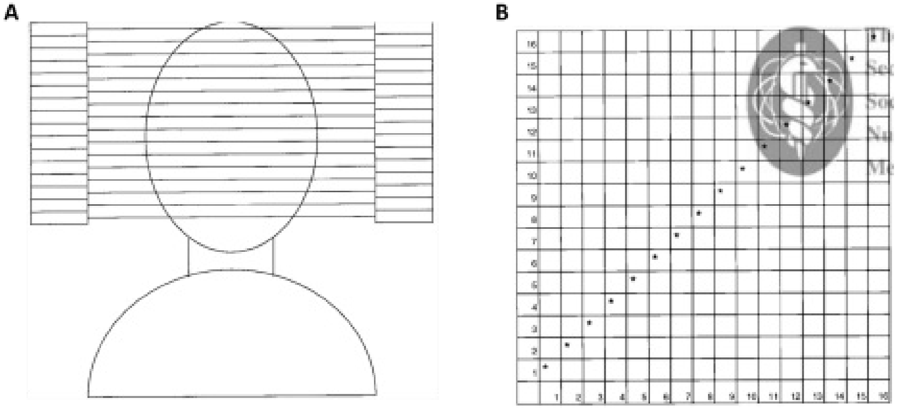

Figure 2.15: A) Illustration of lines-of-response in 2D PET. B) Michelogram of a 16-ring scanner for 2D PET (Source: [32])

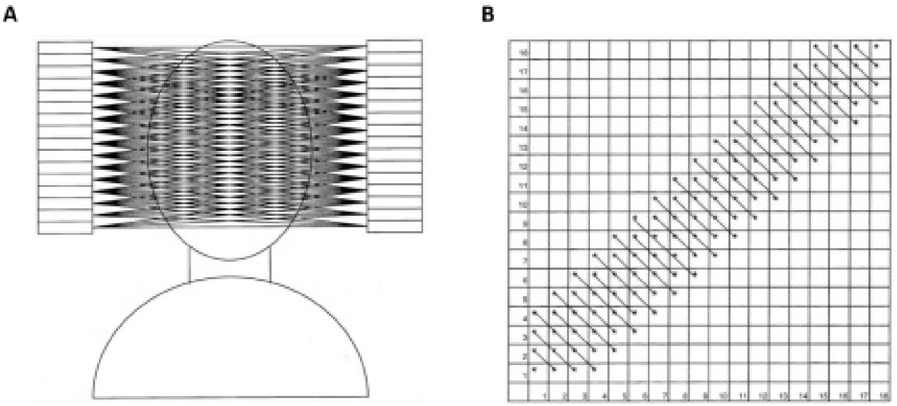

Figure 2.16: A) Illustration of lines-of-response in 3D PET B) Michelogram of a 16-ring scanner used in 3D PET, utilizing a span of 7 (Source: [32])

2.4 Preclinical Imaging

Although basic principles of preclinical and clinical PET scanners are the same, some distinguishing features should be pointed out. Smaller scanner diameters, for example, lead to higher scanner sensitivity [4]. Scatter and attenuation are commonly lower, as photons travel through a thinner layer of matter in mice and rats than in humans. As in clinical imaging, preclinical PET scanners can be combined with MR scanners to get more anatomical information about the subject. Due to the smaller coil diameters in preclincal MR scanners, the magnetic fields currently achievable are much higher than in clinical scanners. As a result, the Lorentz force causes positrons to travel higher distances between emission and annihilation along the scanner axis. Therefore, positron range effects have a higher influence.

2.4.1 Animal Handling

Depending on the area of investigation, rats and mice are predominantly used in preclinical imaging. Especially mice are favorable, as they show not only genetical similarity to humans, also housing- and feeding costs are low because of their fast breeding cycle and small size. In neuroscience, however, rats are more suitable than mice because of their larger brain. Apart from lower resolution being sufficient to visualize structures in the brain, also surgical interventions are performed more easily. As the examinations of animals have to be performed under different circumstances than those of humans, other factors have to be considered, naming anesthesia, temperature or injected volume and activity as examples.

Before imaging, animals have to be put under anesthesia, not only to ensure as little motion as possible, but also because stress and discomfort have to be kept at a justifiable level. It has to be taken into account, however, that anesthetics can have a non negligible influence on the subject's physiology, for example affecting myocardial glucose metabolism, radiotracer uptake in the brain or in tumor cells [3]. As another consequence of anesthesia, mice and rats adapt their body temperature to the ambiance, which can lead to their death. In addition, hypothermia also has an impact on physiology, which is why sufficient heat support has to be provided during imaging.

Despite animals not being subject to the same radiation protection regulations as humans, the administered activity can't be increased arbitrarily to receive good count rate statistics. Apart from technical scanner limitations (dead time originating from scintillation and/or from data processing), physiology has to be kept in mind once again. Moreover, the administered activity is limited by the injectable volume. At an average total blood volume of 2.5 mL, the maximum injectable amount is 0.25 mL [4].

2.5 Monte Carlo Simulations

Complex processes, for which a direct model can't be established, are often simulated using so called Monte Carlo simulations [33]. Those are methods which implement probability theory to find a numerical solution for problems which can't be solved analytically. The simulation methods were named after the famous Casino of Monte Carlo, Monaco, as the outcome of games in a Casino is also based on probability theory. More specifically, Monte Carlo applications make use of known probability density functions to model the underlying system and physical processes involved. Consequently, random numbers are then generated which follow those models.

Monte Carlo simulations bear the benefit, that parameters can be changed rather easily and the effects of those adjustments can be assessed and compared directly. Furthermore, also physically immeasurable quantities, such as the number of scattered events, can be determined. As for the simulation, the origin and entire path of each particle interacting with the detector is known, and straightforward event classification can be conducted.

A priori information, like equations for cross sections of collisions or types of interactions, need to be utilized to make decisions at random which follow models for physical processes. With that, a stochastic variable which obeys a probability function, is generated. For example, photon path lengths can be calculated from random numbers by using the "Distribution function method", explained in [9]. There, the probability, that a photon travels a distance dx is given by:

$$p(x)\,\mathrm{d}x = \mu \exp(-\mu x)\,\mathrm{d}x, \tag{2.11}$$

where μ is a function of the cross section for photon interaction with surrounding material. The probability for a photon to travel the discance d or less is then given by:

$$\mathrm{cpdf}(d) = \int_0^d \mu\, \exp(-\mu x)\,\mathrm{d}x = [-\exp(-\mu x)]_0^d = 1 - \exp(-\mu d) \tag{2.12}$$

The obtained cumulative probability density function cpdf(d) is then substituted for a random number R and the equation is solved for d to get a distributed random variable.

For the computation of simulation models, software packages are used which execute the calculations described so far. Within this project, GATE was used, which is explained in more detail in the following section.

2.5.1 Simulation Software GATE

GATE is an open source software package that can be used to build models of emission scanners. In principle, the outcome depends on 3 modules: The system's geometry, the models that are used to simulate physical processes and the module imitating the readout process, called "digitizer".

Geometry As the structure of medical scanners of the same type is often similar, so called "systems" are provided in GATE, which dictate a hierarchical composition of components. In PET, for instance, most systems are designed of multiple rings with each ring containing numerous detector blocks, often referred to as modules. For most scanners, the detector blocks consist of several small crystals. Thus, the model consists of multiple layers, where the scanner itself is the first layer, the rings are the second, modules represent the third layer, and pixelated crystals correspond to the last layer of scanner components that can be created in GATE.

When scanner dimensions are known in detail, defining the scanner's geometry itself is a straightforward process. Some limitations and restrictions make it hard, however, to create an exact replica of a system. For instance, GATE calls for some layers to be filled mandatory, for example the volume "module" and its daughter volume "crystal", which would normally represent the pixelated crystals. For scanners utilizing monolythic crystals this means, however, that an artificial layer has to be added to satisfy GATE's requirements, which doesn't represent the scanner's attributes correctly.

Physics From GATE version 7.0 on, the software utilizes so called "built-in physics lists" to simulate physical processes such as radioactive decay or the photoelectric effect. This means, that instead of adding and defining each physical effect manually, a predefined physics list including a set of pre-defined processes can be chosen while additional interactions can still be added.

Digitizer GATE's digitizer is a module to simulate the processing chain from a particle interaction to the readout signal. Along this chain, steps and filters are applied to simulate data handling as realistically as possible. The smallest unit that is handled by the digitizer is called a hit. Hits are interactions a particle undergoes along its trajectory in a sensitive material. A particle can lose parts of its energy at multiple hits instead of losing all its energy at once. All hits within the same sensitive volume are summed into so called "pulses" by a module called "adder". If a particle loses its energy via two steps in two different volumes, for instance, two pulses are generated. There, the energy of each pulse is the sum of all energies emitted in one volume and its position is determined by an energy-weighted centroid of the hit-positions. Subsequently, the signal is processed by the readout-module which corresponds to the photo detectors utilized in the real system.

2.6 Performance Measurements

Performance measurements are a standardized methodology to compare scanners among each other and also to assess their ability of carrying out specific imaging applications [15]. The standard used within this work ”NEMA NU4-2008” was developed by the ”Electrical Manufacturers Association”. In this chapter an overview of the matter, based on [21] is given. For details on all definitions the reader is referred to [15].

Sensitivity The absolute sensitivity of a PET scanner is specified by the ratio of detected counts versus the total activity present in the FOV. It is given by the formula

$$S = \frac{R_{\mathrm{prompt}} - R_{\mathrm{background}}}{A}, \tag{2.13}$$

where S denotes the sensitivity in percent, R_{prompt} is the count rate of prompt events, $R_{background}$ is the count rate of background events and A denotes the activity present in the Field of View. The absolute sensitivity is obtained by accounting for the branching ratio of a nuclide. As ^{22}Na decays via β^+ emission in 90.6 % of cases, the value for the absolute sensitivity using a ^{22}Na source is obtained via

$$S_A = S \cdot 0.906 \tag{2.14}$$

A scanner’s sensitivity is determined by multiple factors, such as the type of detector used, amount of dead space (meaning the slits between crystals where no photons can be detected), crystal thickness and the solid angle coverage with sensitive detectors. Also geometrical attributes have an influence on sensitivity: Normally, longer axial

FOV and smaller bore diameters lead to higher sensitivity [3].

Noise Equivalent Count Rate and Scatter Fraction There are various ways to handle scatter- or random coincidences within a scanner. Therefore, to be able to compare scanners among each other, the *Noise Equivalent Count rate (NEC)* is examined. It is the count rate that would lead to the same signal-to-noise ratio if no random or scattered events were present. The true count rate R_{true} is calculated as follows:

$$R_{\text{true}} = R_{\text{prompt}} - R_{\text{scatter}} - R_{\text{random}}, \tag{2.15}$$

where R_{prompt} is the detected count rate of prompt events, R_{scatter} is the count rate of scattered events and the rate of detected random events is called R_{random}. Subsequently, the NEC-count rate $NECR$ is defined as

$$NECR = \frac{{R_{\text{true}}}^2}{R_{\text{true}} + aR_{\text{scatter}} + bR_{\text{random}}}, \tag{2.16}$$

where a is the "...fraction of the projection that is occupied by the object being imaged", [21]. The constant b is dependent of the method used for random estimation. If the singles method (see section 2.2) is used (which is the case for our scanner), $b = 1$. Because of deadtime effects originating from the scintillation process as well as from data processing, the number of events a scanner can process per unit time is limited. This means that the number of detected events doesn't depend linearly on activity and even drops again above a certain value. Activities exceeding the activity at which the peak count rate occurs are not represented appropriately anymore, hence limiting the maximum administered activity to a subject which can still be imaged without bias.

A scanner's *Scatter Fraction (SF)* is the ratio of scattered events to the sum of scattered and true events,

$$SF = \frac{R_{\text{scatter}}}{R_{\text{true}} + R_{\text{scatter}}} \tag{2.17}$$

The amount of scattered events strongly depends on the probe being examined because more material surrounding the radioactive source distribution leads to a more likely deviation of photons. For mouse and rat scans, typical scatter fractions are ≈8 % and ≈20 %, respectively [3]. In preclinical research, the imaging of multiple animals at the same time is often desirable. Through that, not only time can be saved, also the application of short-lived radiotracers is possible in a more economic way. As scatter fractions increase by 25 % to 64 % [3], simulating the scanner and subject setup could be beneficial to limit scatter effects by optimizing the measurement setup.

Spatial Resolution The minimum distance for two points being identified as separate is called "Spatial resolution". One way to give this value is as **Full Width at Half Maximum** (FWHM). This is the interval between the x-values where the system response to a point source reaches half the maximum function value. A visualization can be found in figure 2.17. The "Full Width at Tenth Maximum" is calculated accordingly at a tenth of the maximum function value.

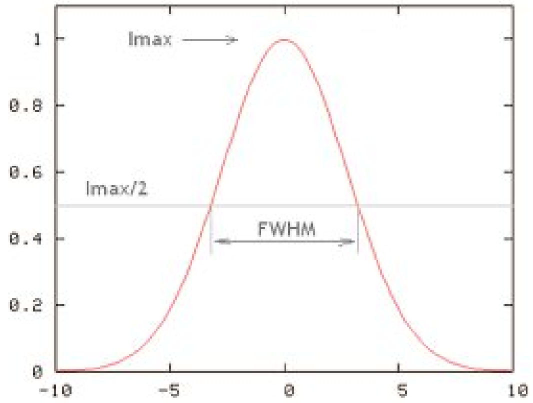

Figure 2.17: Representation of a Full Width at Half Maximum: The distance between the rising and falling function-values at exactly half of its maximum. (Source: [34])

Preclinical scanners show a spatial resolution of approximately 1.5 mm to 2.5 mm FWHM [3]. A scanner's spatial resolution strongly depends on the radial distance from scanner center, with smaller values close to center increasing towards the edges of the FOV. This effect is more prevalent in scanners with smaller bore sizes [3].

Image Quality To be able to compare scanners amongst each other and to assess the interaction of parameters, a standardized imaging situation, performed with a specific phantom, is used to evaluate the image quality of systems. An illustration of the image quality phantom used can be seen in figure 3.4. In the following, explanations for the informative value of measured values are given based on [15]. A detailed explanation on how those values are determined can be found in section 3.3.

To get an idea of the spatial resolution in an imaging situation, recovery coefficients are determined for objects, filled with activity with different sizes. A scanner's uniformity is indicative for its attenuation and scatter correction performance. Furthermore, scatter correction performance can be evaluated by activity measurements within regions without activity which are positioned inside a region containing activity.

3. Materials and Methods

3.1 The PET Insert

The evaluated preclinical PET insert, model "Si 198" was manufactured by the Bruker Biospin GmbH, Germany. An illustration can be found in figure 3.1 a). The insert can be coupled with preclinical MR scanners. At the Medical University of Vienna, the insert is placed inside a preclinical MR scanner, the 9.4 T MR model "BioSpec® 94/30", which is also manufactured by the Bruker Biospin GmbH.

The scanner consists of 3 rings, each of which contains 8 modules. All modules enclose a monolythic LYSO crystal with a thickness of 10 mm. While the patient-faced surface is 48 mm × 48 mm big, the outward faced side measures 50 mm × 50 mm. The inner detector distance measures 11.4 cm, the outer diameter of the PET insert is 19.8 cm. For light amplification, 144 silicon photomultipliers are coupled to each detector crystal. This setup allows to observe a field of view (FOV) of 80 mm × 80 mm × 150 mm. Figure 3.1 b) contains a transaxial sectional view of a scanner ring and the trapezoidal detectors.

Different patient tables are available, suitable for the different subject-sizes being observed. At General Hospital of Vienna (AKH), the patient table is a hollow half-cylinder made of high density polyethylene cut along the central axis. It has an inner diameter of 13 mm, an outer diameter of 17 mm and measures 150 mm in height. A depiction of the patient table can be found in figure 3.3.

3.1.1 Performance Measurements

The measurements for sensitivity, spatial resolution, noise equivalent count rate (NEC) and image quality were performed following the NEMA NU 4-2008 standard

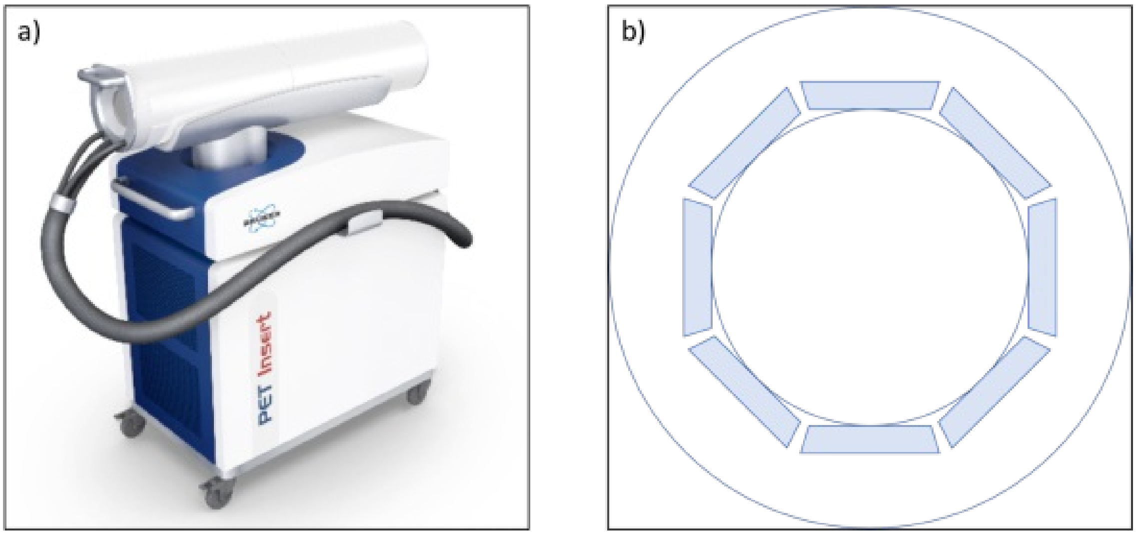

Figure 3.1: a) The PET-Insert as presented on the Bruker homepage. The insert comes on a mobile cart. (Source: [35]) b) Transaxial sectional view of a scanner ring of the Bruker PET Insert "Si 198". Note the trapezoidal shape of the monolythic crystals.

for preclinical PET scanners [15] and are explained in more detail below.

Sensitivity A ^{22}Na point source with a diameter of ≈0.25 mm, embedded inside an acrylic cube with a size of 1 cm × 1 cm × 1 cm, was used for the sensitivity measurements. Calibrated at Seibersdorf Laboratories on 01.08.2018 with 383.3 kBq, the source had an activity of 232.3 kBq at the time of measurement. Being located in the transaxial center, the point source was stepped axially through the entire FOV, starting at −75.2 mm axial distance from center to 76.1 mm axial distance. The scanner's positioning system employs a stepper motor with which a continuous stepsize can't be set. Therefore, the distance between measurements varies within (2.0 ± 0.3) mm. All values are given in the appendix in table A.1. At each position, counts were acquired for 10 s. A background scan was performed, meaning data acquisition was started without a source being present at the FOV.

Noise Equivalent Count Rate (NEC) Measurements for prompt, scatter, random and noise equivalent count rate were performed with two different phantoms to resemble a mouse- and a rat-body. A picture of the mouse-sized cylinder can be found in figure 3.2. Both are cylinders made of high-density polyethylene to cause scattering of annihilation photons. While the mouse-sized cylinder measures 70 mm

Figure 3.2: Mouse-sized phantom for scatter-measurements based on NEMA-standards. A high density polyethylene cylinder holds the line source, which is created by filling flexible tubing with [^{18}F]FDG. (Source: [37])

in length and 25 mm in diameter, the rat sized phantom is 150 mm long and of 50 mm diameter. Both phantoms include a cylindrical hole of 3.2 mm diameter parallel to the central axis with a distance of 10 mm (mouse) or 17 mm (rat) to center. A line source was created in both cases, by filling flexible tubing with 40.48 MBq (mouse) and 53.04 MBq (rat) [^{18}F]FDG mixed with saline solution. The tubing was filled up to a region 10 mm shorter than the corresponding cylinder-phantom and inserted centered into the cylinders. Plastic screws were used for closing the sources. Each cylinder was placed centered inside the scanner seperately with the line source facing towards the mouse bed, shown in figure 3.3. For measurements, counts were acquired for 60 s every 10 min repeatedly for 100 times. This was realized by selecting the PET-acquisition protocol ”PET - test NECR”, supplied by the vendor, as suggested in [36].

Spatial Resolution The same ^{22}Na point source that was employed for sensitivity assessment was used to perform sensitivity measurements. The activity was 232.3 kBq at the time of measurement. First, the source was placed at the axial center of the FOV and stepped transaxially to 5 mm, 10 mm, 15 mm and 25 mm distance from center. Subsequently, the source was fixed at $\frac{1}{4}$ of the axial FOV, meaning at 37.5 mm axial distance from center and stepped to the same transaxial distances again. At each point, data acquisition was carried out for 60 s. At the scanner software, ^{22}Na was selected as ”compound”, which results in an energy

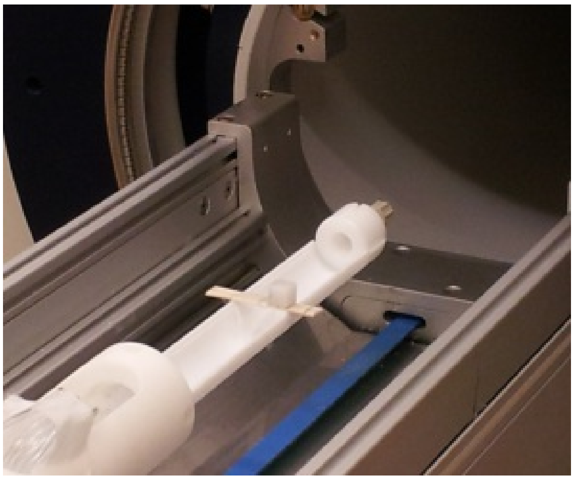

Figure 3.3: Picture of actual measurement setup for spatial resolution tests. A ^{22}Na point source, embedded in an acrylic cube is placed on the scanner's patient table and stepped transaxially through the field of view.

window of 357.7 keV to 664.3 keV for the measurement. A picture of the real spatial resulution measurement setup can be found in figure 3.3.

The NEMA NU 4-2008 standard suggests filtered back projection (FBP) of raw data for evaluation of spatial resolution. This was carried out using an inhouse developed Matlab script. Matlab version R2018a, including the image processing toolbox was used. It provides a function that performs inverse Radon-transformation based on the sinogram and a few parameters and is called "iradon". Each slice of the obtained sinograms was given separately to the function, together with a vector containing all angles from which the projections were acquired. Corresponding to the pixel size in the sinograms, the angle step size was selected as 0.93747 °. A conventional Ram-Lak filter with the shape of a ramp (see section 2.3.1) was applied as it shows best results for spatial resolution [38]. A frequency scaling of 1 was selected and a pixel size of 320 × 320 for each backprojected image was chosen. Thus, the image matrix of all backprojected images cosisted of 320 × 320 × 150 voxels with a size of 0.25 mm × 0.25 mm × 1 mm.

Image Quality The phantom used to assess image quality is a cylinder made of polymethyl methacrylate (PMMA) divided in different sections. To be able to visualize the physical appearance of the image quality phantom, an illustration of it can be found in figure 3.4. Its total length measures 63 mm and its outer diameter is 33.5 mm. The first section, called "uniform region" (UR), has an inner diameter and a length of 30 mm and is filled with liquid isotope. Two "cold zones" (meaning zones without activity) are placed inside the UR by being included into the lid: a water filled cavity and an air filled cavity. They both have an inner diameter of 8 mm at a length of 15 mm and a wall thickness of 1 mm, with their centers being 15 mm apart. The second part of the phantom consists of solid PMMA including 5 holes drilled into it parallel to the central axis. Thereby, 5 rods with the diameters of 5 mm, 4 mm, 3 mm, 2 mm and 1 mm were formed, all of them measuring 20 mm in length. Adjacent to the rods, a 3 mm long and 20 mm wide cylinder containing activity is placed. The phantom can hold a volume of 20.66 mL and was filled with an activity of 3.48 MBq for the measurement, resulting in an activity concentraction of 0.17 MBq mL^{-1}.

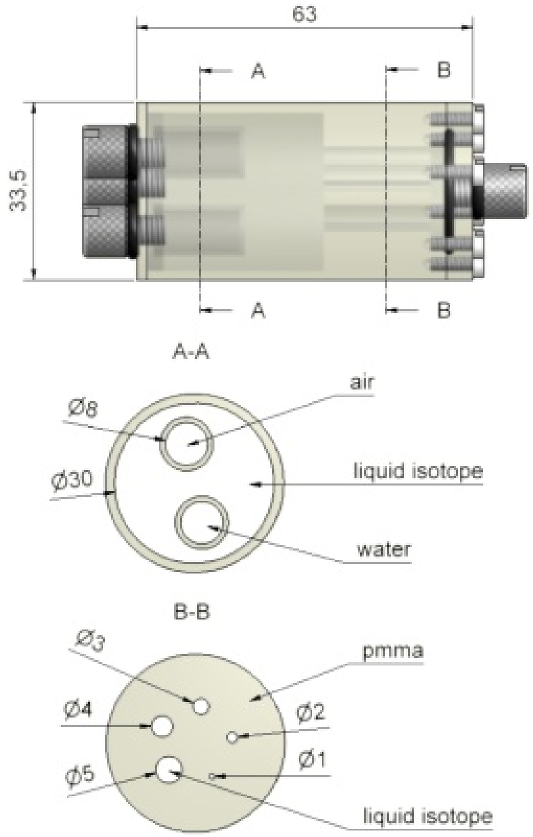

Figure 3.4: Side view and cross sections of the image quality phantom. Source: [37]

Acquisition and Reconstruction Settings Selected configurations for acquisition times, corrections applied, compounds selected and corresponding energy windows can be found in table 3.1. Where necessary (sensitivity, NEC, spatial resolution), sinograms where obtained with a software specifically provided by Bruker ("lmSinogramCreator"). This process is described in the manual *Performance Evaluation Based on NEMA-NU-2008 In Manufacturing process* supplied by the vendor. A virtual pixel size has to be specified which is then used to rearrange the data into sinograms. For this work, a virtual voxel size of 1 mm × 1 mm × 1 mm was selected. The sinogram creator additionally performs single slice rebinning on the sinograms, which eventually consist of 168 × 193 × 150 voxels. Here, the voxel size was 0.479 mm × 0.016 rad × 1 mm. Aside from sinograms with prompt count rate, the vendor-supplied software also produces sinograms containing the estimated random count rate. Those sinograms have the same size and pixel size as "prompt" sinograms. No smoothing was applied to the sinograms.

For the image quality measurements, the scanner workstations' software was used to reconstruct the images. There, a chosen voxel-size of 0.25 mm × 0.25 mm × 0.25 mm led to an image matrix of 320 × 320 × 600 voxels.

Measurement	compound	energy window [keV]	acquisition time [s]	decay correction	deadtime correction	normalization correction	attenuation correction	scatter correction
Spatial Resolution	Na-22Ap	357.7 - 664.3	60	no	yes	yes	no	no
Sensitivity	F-18 51A	250.39 - 771.61	10	no	yes	yes	no	no
NEC - mouse	F-18 51A	250.39 - 771.61	60	no	yes	yes	no	no
NEC - rat	F-18 51A	250.39 - 771.61	60	no	yes	yes	no	no
Image Quality	F-18	357.7 - 664.3	1200	yes	yes	yes	no	yes

Table 3.1: Reconstruction settings selected on the scanner software.

3.2 The Monte Carlo Model of the PET Insert

The simulation model of the PET system was created following the system specifications described in section 3.1. The GATE version 8.0 (GEANT4 10.3.2) was used. Rigid GATE restrictions regarding crystal shape and the system layers make it necessary, however, to deviate from those specifications a little. As GATE requires the crystals to be of cuboid shape and not trapezoidal like in the real system, they were simulated with a size of 48 mm × 48 mm × 10 mm, thus the axial length of the system stays the same. Similar to [7], custom made LYSO with a density of $7.3\,\mathrm{g\,cm^{-3}}$, composed of 22.5 % Lutetium, 2.5 % Yttrium, 12.5 % Silicon and 62.5 % Oxygen was utilized (GATE settings A, table 3.2). For comparison, another type of LYSO with the same density of $7.3\,\mathrm{g\,cm^{-3}}$, composed of 36 % Lutetium, 4 % Yttrium, 10 % Silicon and 50 % Oxygen was simulated (GATE settings B, table 3.3).

Apart from that, a GATE layer's daughter layer includes its physically next smaller unit, for example a "module" would include its "crystals". As the Bruker PET Insert uses monolythic crystals, the last utilized layer would be the "module". To enable data acquisition and analysis in GATE however, all mandatory layers have to be filled. Thus, the virtual pixels mentioned in section 3.1.1 were realized as an additional layer even though they are not separated physically in the real system. A visualization of the created model can be found in figure 3.5.

To keep computation times on a reasonable level, sensitivity measurements were simulated at 32 positions instead of 78. NEC-measurements were simulated at 13 activities for the mouse-sized phantom and 20 for the rat-sized one. For spatial resolution measurements, all acquisition positions were simulated.

Sources and Phantoms Geometric properties of all phantoms were simulated to match the real phantoms' dimensions. The NEC-cylinders were both modeled to be made of Polyethylene with a density of $1.06\,\mathrm{g\,cm^{-3}}$ and (C_2H_4). The acrylic cube utilized for spatial resolution and sensitivity measurements was simulated to be of "Plastic" with a density of $1.18\,\mathrm{g\,cm^{-3}}$ and ($C_5H_8O_2$).

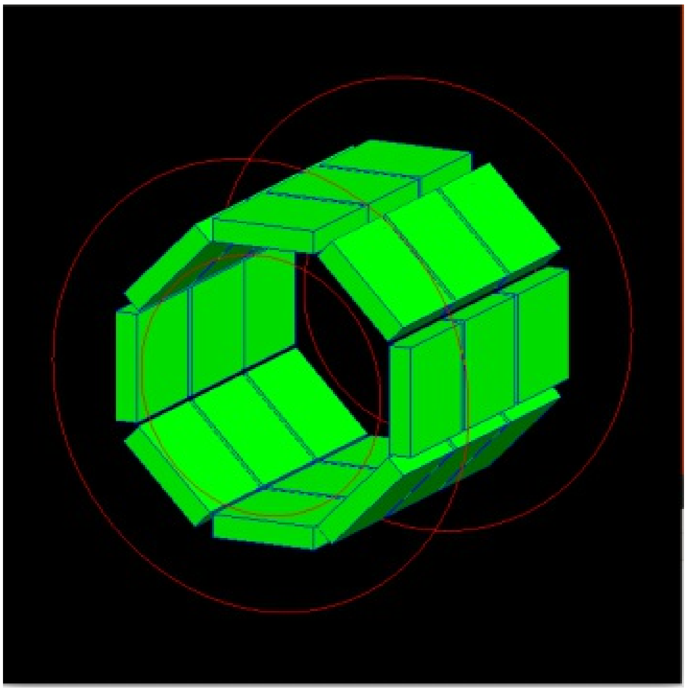

Figure 3.5: Visualization of the GATE model of a preclinial PET Insert ”Si 198”, manufactured by Bruker BioSpin GmbH.

Physics Physical processes in GATE were modeled using a built-in physics list called ”empenelope”. Additionally, radioactive decay, atom de-excitation and positron annihilation were enabled. In GATE, cuts for photons, electrons and positrons specify the range below which those particles don’t produce secondary effects. They have to be given for each relevant region in the GATE system. Within this work, the cuts in the crystal and the phantom region were set to 10 keV for positrons and photons and to 1 mm for electrons.

Digitizer The readout behavior ”TakeEnergyWinner” was chosen at the readout depth one. An energy filter, depending on the isotope and measurement type was implemented and its values are congruent with those from table 3.1. A gaussian energy blurring of 17 % FWHM at 511 keV and a gaussian time blurring of 5 ns were applied. These values were chosen comparable to [39] and [7] as the detector configuration is similar. On the singles level (equivalent to the crystal level in the real system), a paralysable dead time of 850 ns was applied. It is noteworthy, that deadtime on crystal level as well as on readout electronics level contribute to the scanner deadtime. GATE is capable of simulating this setup, however, this was not exploited as more specific information was not available. Singles thus obtained were sorted into "Coincidences" utilizing a coincidence window of 7 ns. To be able to assess the random count rate, a delayed coincidence window was added with an offset of 200 ns. All values are summarized in table 3.2. Quantum efficiency, crosstalk and buffer size effects were not modeled in the course of this project, as such information is scanner specific and could not be obtained from reliable sources.

		NEC Rat	**NEC Mouse**	**Sensitivity**	**SpRes**
Phantom	**Material**	Polyethylene ($C2H4$)	Polyethylene ($C2H4$)	Plastic ($C5H8O2$)	Plastic ($C5H8O2$)
	Density	1.06 g cm^{-3}	1.06 g cm^{-3}	1.18 g cm^{-3}	1.18 g cm^{-3}
Lu2(1-x)Y2xSiO5	**Material**	Lu 1.8 Y 0.2 Si O 5	Lu 1.8 Y 0.2 Si O 5	Lu 1.8 Y 0.2 Si O 5	Lu 1.8 Y 0.2 Si O 5
	Density	7.3 g cm^{-3}	7.3 g cm^{-3}	7.3 g cm^{-3}	7.3 g cm^{-3}
Source	**Type**	ion	back to back	ion	ion
	Initial Activity	53.04 MBq	40.48 MBq	232 kBq	232 kBq
Physics	**Physics list**	empenelope	empenelope	empenelope	empenelope
	Processes	Radioactive Decay	Radioactive Decay	Radioactive Decay	Radioactive Decay
		Atom Deexcitation	Atom Deexcitation	Atom Deexcitation	Atom Deexcitation
		Positron Annih.	Positron Annih.	Positron Annih.	Positron Annih.
Cuts Phantom	**Photons**	10 keV	10 keV	10 keV	10 keV
	Electrons	0.1 cm	0.1 cm	0.1 cm	0.1 cm
	Positrons	10 keV	10 keV	10 keV	10 keV
Cuts Crystal	**Photons**	10 keV	10 keV	10 keV	10 keV
	Electrons	0.1 cm	0.1 cm	0.1 cm	0.1 cm
	Positrons	10 keV	10 keV	10 keV	10 keV
Readout	**Readout Policy**	TakeEnergyWinner	TakeEnergyWinner	TakeEnergyWinner	TakeEnergyWinner
	Readout Depth	1	1	1	1
EnergyBlurring	**Reference**	511 keV	511 keV	511 keV	511 keV
	FWHM	17.00%	17.00%	17.00%	17.00%
EnergyWindow	**Threshold**	250.39 keV	250.39 keV	250.39 keV	357.7 keV
	Uphold	771.61 keV	771.61 keV	771.61 keV	664.3 keV
Timing Resolution	**Time Resolution**	5 ns FWHM	5 ns FWHM	5 ns FWHM	5 ns FWHM
SingleDeadtime	**Volume**	module	module	module	module
	Mode	paralysable	paralysable	paralysable	paralysable
	Value	850 ns	850 ns	850 ns	850 ns
Coincidences	**Window**	7 ns	7 ns	7 ns	7 ns
	Offset	200 ns	200 ns	200 ns	200 ns
	Multiples Policy	killAll	killAll	killAll	killAll
Patient Table	**Material**	Polyethylene ($C2H4$)	Polyethylene ($C2H4$)	Polyethylene ($C2H4$)	Polyethylene ($C2H4$)
	Density	1.06 g cm^{-3}	1.06 g cm^{-3}	1.06 g cm^{-3}	1.06 g cm^{-3}
	Rmin	13 mm	13 mm	13 mm	13 mm
	Rmax	17 mm	17 mm	17 mm	17 mm
	Length	150 mm	150 mm	150 mm	150 mm
	Phi Start	180 deg	180 deg	180 deg	180 deg
	DeltaPhi	180 deg	180 deg	180 deg	180 deg

Table 3.2: GATE-Settings - A

		NEC Rat	**NEC Mouse**	**Sensitivity**	**SpRes**
Phantom	**Material**	Polyethylene (C2H4)	Polyethylene (C2H4)	Plastic (C5H8O2)	Plastic (C5H8O2)
	Density	1.06 g cm^{-3}	1.06 g cm^{-3}	1.18 g cm^{-3}	1.18 g cm^{-3}
Lu2(1-x)Y2xSiO5	**Material**	Lu 1.8 Y 0.2 Si O 5	Lu 1.8 Y 0.2 Si O 5	Lu 1.8 Y 0.2 Si O 5	Lu 1.8 Y 0.2 Si O 5
	Density	7.3 g cm^{-3}	7.3 g cm^{-3}	7.3 g cm^{-3}	7.3 g cm^{-3}
Source	**Type**	ion	back to back	ion	ion
	Initial Activity	53.04 MBq	40.48 MBq	232 kBq	232 kBq
Physics	**Physics list**	empenelope	empenelope	empenelope	empenelope
	Processes	Radioactive Decay	Radioactive Decay	Radioactive Decay	Radioactive Decay
		Atom Deexcitation	Atom Deexcitation	Atom Deexcitation	Atom Deexcitation
		Positron Annih.	Positron Annih.	Positron Annih.	Positron Annih.
Cuts Phantom	**Photons**	10 keV	10 keV	10 keV	10 keV
	Electrons	0.1 cm	0.1 cm	0.1 cm	0.1 cm
	Positrons	10 keV	10 keV	10 keV	10 keV
Cuts Crystal	**Photons**	10 keV	10 keV	10 keV	10 keV
	Electrons	0.1 cm	0.1 cm	0.1 cm	0.1 cm
	Positrons	10 keV	10 keV	10 keV	10 keV
Readout	**Readout Policy**	TakeEnergyWinner	TakeEnergyWinner	TakeEnergyWinner	TakeEnergyWinner
	Readout Depth	1	1	1	1
EnergyBlurring	**Reference**	511 keV	511 keV	511 keV	511 keV
	FWHM	17.00%	17.00%	17.00%	17.00%
EnergyWindow	**Threshold**	250.39 keV	250.39 keV	250.39 keV	357.7 keV
	Uphold	771.61 keV	771.61 keV	771.61 keV	664.3 keV
Timing Resolution	**Time Resolution**	5 ns FWHM	5 ns FWHM	5 ns FWHM	5 ns FWHM
SingleDeadtime	**Volume**	module	module	module	module
	Mode	paralysable	paralysable	paralysable	paralysable
	Value	850 ns	850 ns	850 ns	850 ns
Coincidences	**Window**	7 ns	7 ns	7 ns	7 ns
	Offset	200 ns	200 ns	200 ns	200 ns
	Multiples Policy	killAll	killAll	killAll	killAll
Patient Table	**Material**	Polyethylene (C2H4)	Polyethylene (C2H4)	Polyethylene (C2H4)	Polyethylene (C2H4)
	Density	1.06 g cm^{-3}	1.06 g cm^{-3}	1.06 g cm^{-3}	1.06 g cm^{-3}
	Rmin	13 mm	13 mm	13 mm	13 mm
	Rmax	17 mm	17 mm	17 mm	17 mm
	Length	150 mm	150 mm	150 mm	150 mm
	Phi Start	180 deg	180 deg	180 deg	180 deg
	DeltaPhi	180 deg	180 deg	180 deg	180 deg

Table 3.3: GATE-Settings B

3.2.1 Image Reconstruction for Monte Carlo Simulated Data

To obtain images and sinograms from GATE-generated ASCII files, OMEGA version 1.1.0, an Open-source MATLAB Emission Tomography Software [40], was used. A span of 143 was selected (see section 2.3.3) while the maximum ring difference was set to 143 for all configurations. The number of radial positions in the sinograms was set to 168. Even though the real system uses 193 angles per sinogram, in OMEGA this number was set to 192 as it was the maximum selectable value. Those settings resulted in a sinogram size of $168 \times 192 \times 573$ pixels. OMEGA was also used to retract sinograms containing exclusively random counts. To match the measurement settings, neither random, scatter nor attenuation correction were performed. Differing from the real measurements, no normalization correction was carried out, as no data was retractable from OMEGA or GATE for this purpose.

3.3 Data Analysis

The analysis of data was performed following the NEMA protocol, identically for GATE and for real measurements. Matlab scripts were developed, with Matlab version R2018a including the image processing toolbox. The procedures are described in detail below and minor differences are stressed where applied.

Sensitivity Sensitivity evaluation was based on sinograms, following the NEMA standard. A summary of the procedure is given below. For each slice, the maximum pixel per row was located and a mask was applied. With it, all pixels outside a 2 cm strip were set to zero. Subsequently, all pixels of the sinogram were added to receive the total count number per slice. For the sinograms obtained from GATE-simulations, the number was then divided by the acquisition time to receive a count rate. This was, however, not necessary for sinograms produced by the real scanner, as those are automatically averaged over acquisition time. According to the NEMA-protocol, the background count rate (see section 2.1.3 for explanation) should now be subtracted from the real count rate. As explained above this procedure could not be followed, as non numerical values were obtained for such measurements. Therefore, neither for GATE, nor for real measurements the background rate was taken into account. To further correct for positron branching ratio of ^{22}Na (90.6 %), the result obtained was then divided by 0.906. The total absolute scanner sensitivity was calculated by averaging over all positions.

Noise Equivalent Count Rate In adherence to the NEMA protocol, a mask was applied to each sinogram obtained for NEC measurements. Again, for each slice, the maximum pixel per row was located and a mask was applied. This time, pixels further than 8 mm away from phantom borders were set to zero. Then the rows for each slice were shifted, such, that the pixel with the maximum value was located in the central pixel of each row. Subsequently, all rows were summed to create an object which is referred to as the "sum projection". The purpose of the measurements in this section is to identify scattered or random from true counts. Outside a certain border around the line source, it can be assumed that all counts are scattered or random. Accordingly, for each sum projection (that is, essentially, for each slice) the two pixels just inside the ±7 mm borders are used to fit a straight line above which counts are interpreted as "true". All counts below that line are assumed to originate from scattered events. Random count rate estimation was performed based on random-sinograms for real measurements as well as for GATE measurements.

Spatial Resolution To assess the spatial resolution, images reconstructed with FBP were used for analysis, as described by the NEMA protocol. Here, the procedure was to detect the maximum pixel within the three-dimensional image matrix, and three line profiles were placed through it, parallel to every dimension. This way, three vectors were received for all measurements, each containing counts per pixel per row, column and slice of the maximum pixel. Using the maximum pixel and its direct neighbors as supporting points, a quadratic function was fitted. The distance between the x-values for which the function reaches half its maximal value is called full width at half maximum (FWHM) and is the value for spatial resolution.

Image Quality As for all other performance measurements, data analysis for image quality was performed as described in the NEMA standard. For viewing images, drawing volumes of interest (VOIs) and performing statistic calculations, the software "AMIDE", version 1.0.4 was used [41]. Within the image quality assessment, three analyses were performed: uniformity assessment, recovery coefficients and accuracy of corrections.

For uniformity assessment, a 10 mm long and 22.5 mm wide cylinder was drawn over the center of the uniform region and the following values were measured and reported: average activity concentration, maximum and minimum values within the VOI as well as percentage standard deviation.

Recovery coefficients (RC) are the ratio of measured activity inside the rods with different diameters to the expected activity, which is measured in the uniform region. This means RCs are a measure for how well the actual activity present in each rod can be recovered, or else they "[...] are indicative of the spatial resolution of the imaging system." [15]. Rod-diameters, for which the RC is close to one, can be resolved well by the scanner, while rods with RCs close to zero can hardly be detected. To determine the recovery coefficients for the activity filled rods, first the image slices covering the central 10 mm of the rods were averaged to obtain a single image slice with lower noise. Then, circular regions of interest (ROI) were drawn around each rod with double the diameter compared to the respective rod. For all of those ROIs the maximum values were determined. Subsequently, line profiles, parallel to the axial direction of the phantom, were placed through each maximum pixel of the rods. The recovery coefficient (RC) for each rod is then represented by the ratio of the mean of all values along each line profile to the mean activity concentration which was determined in the uniformity test. The standard deviation of the recovery coefficients $\%STD_{\mathrm{RC}}$ was then calculated by the specific formula:

$$\%STD_{\mathrm{RC}} = 100 * \sqrt{\left(\frac{STD_{\mathrm{lineprofile}}}{Mean_{\mathrm{lineprofile}}}\right)^2 + \left(\frac{STD_{\mathrm{background}}}{Mean_{\mathrm{background}}}\right)^2}. \tag{3.1}$$

To evaluate the accuracy of corrections, volumes of interest (VOI) were defined in the air- as well as in the water filled cylinders inside the uniform region. Those VOIs, each having a length of 7.5 mm and a diameter of 4 mm, were placed over the center of the air- and water filled cylinder respectively. The spill over ratio (SOR) denotes the ratio of the mean in each cold region to the mean of the hot uniform area. The standard deviation was then calculated analogous to equation (3.1).

4. Results

4.1 Measurements

4.1.1 Sensitivity

Absolute sensitivity is zero at the edges of the FOV and increases towards the center. As can be seen in figure 4.1, discontinuities appear symmetrically at −48 mm and 48 mm axial distance from center as well as at −24 mm and 24 mm axial distance and −4 mm and 4 mm distance from center. Absolute sensitivity reaches its maximum of 12.53 % at 6 mm distance from center, drops down to 11.67 % at the center of FOV and increases to reach 12.32 % at −6.1 mm again. The evaluated total absolute scanner sensitivity was 7.95 %. A graph can be seen in figure 4.1.

For sensitivity measurements, a background scan was performed as proposed in the NEMA protocol [15], but obtained sinograms only contained non-numerical values. Therefore, an intrinsic background count rate was not taken into account for evaluation of following results.

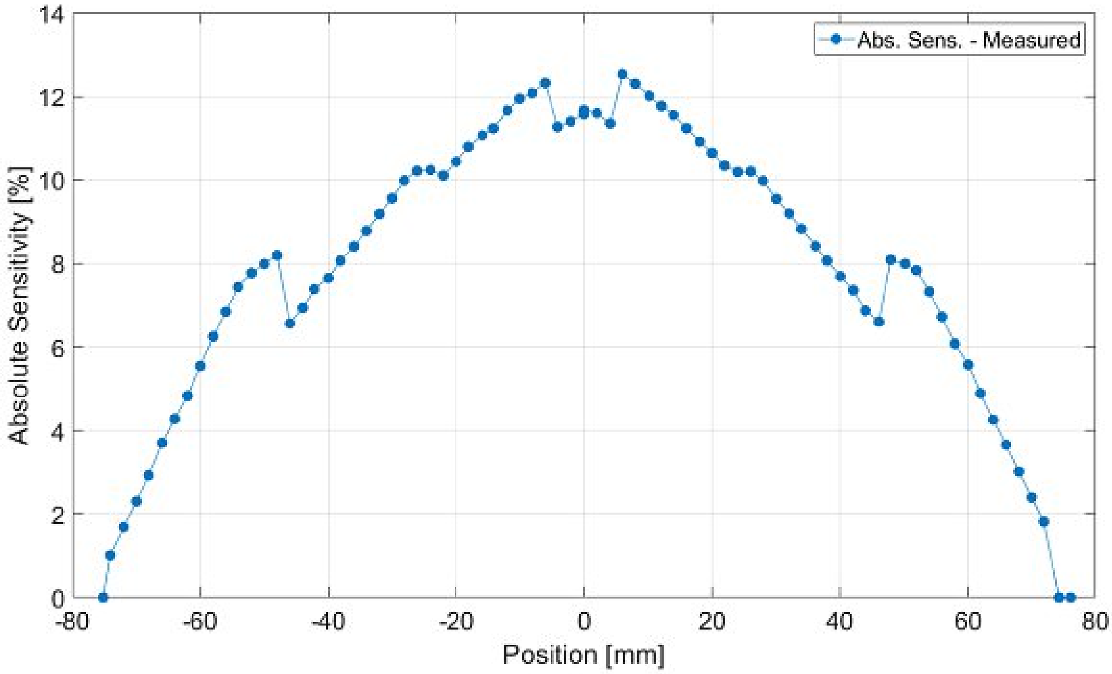

Figure 4.1: Measured absolute scanner sensitivity over axial position – The absolute scanner sensitivity rises towards the center of the FOV. Discontinuities can be observed symetrically around the origin at ±48 mm, ±24 mm and ±4 mm. The highest absolute sensitivities of 12.53 % and 12.32 % are reached at ±6 mm distance from center.

4.1.2 Noise Equivalent Count Rate

For the rat-like phantom, the true count rate reached its maximum of 302 kcps at 28.3 MBq, while the NEC-count rate reached its maximum at 21.43 MBq and was 177 kcps. In the smaller mouse-sized cylinder, the true count rate reached its maximum of 454 kcps at 24.8 MBq. There, the NEC count rate reached up to 361 kcps at 21.6 MBq. Values for prompt, true, NEC, scattered and random events are plotted in figure 4.2 for the mouse-sized cylinder phantom and in figure 4.3 for the rat-sized cylinder. Analogous to sensitivity measurements, also for NEC-measurements background scans were performed as proposed, but didn't produce usable values.

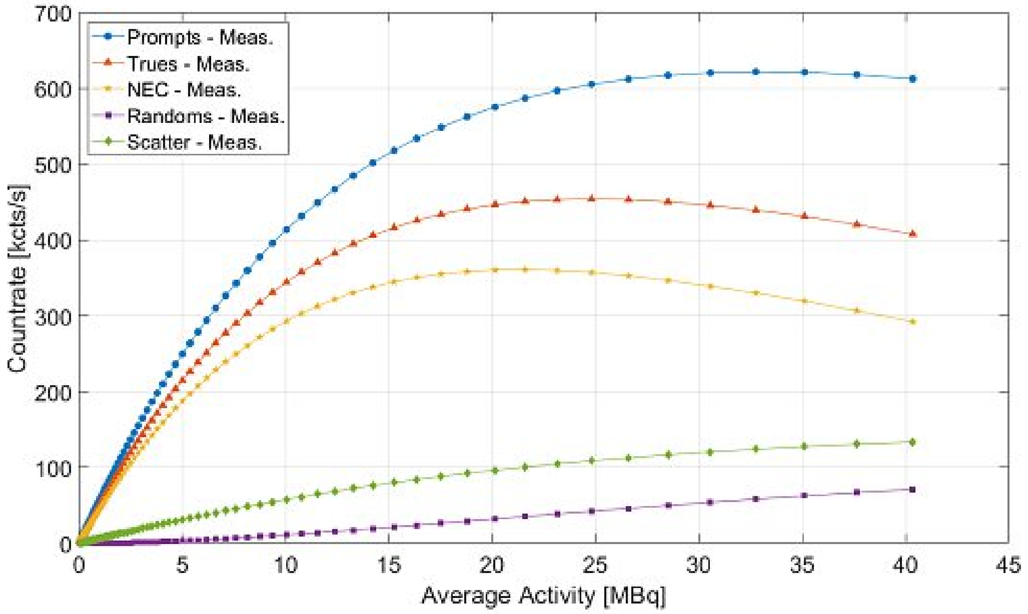

Figure 4.2: Measured countrates for mouse-sized cylinder phantom – The peak NEC count rate reaches its maximum of 361 kcps at 21.6 MBq, while the peak true event count rate reached its maximum of 454 kcps at 24.8 MBq.

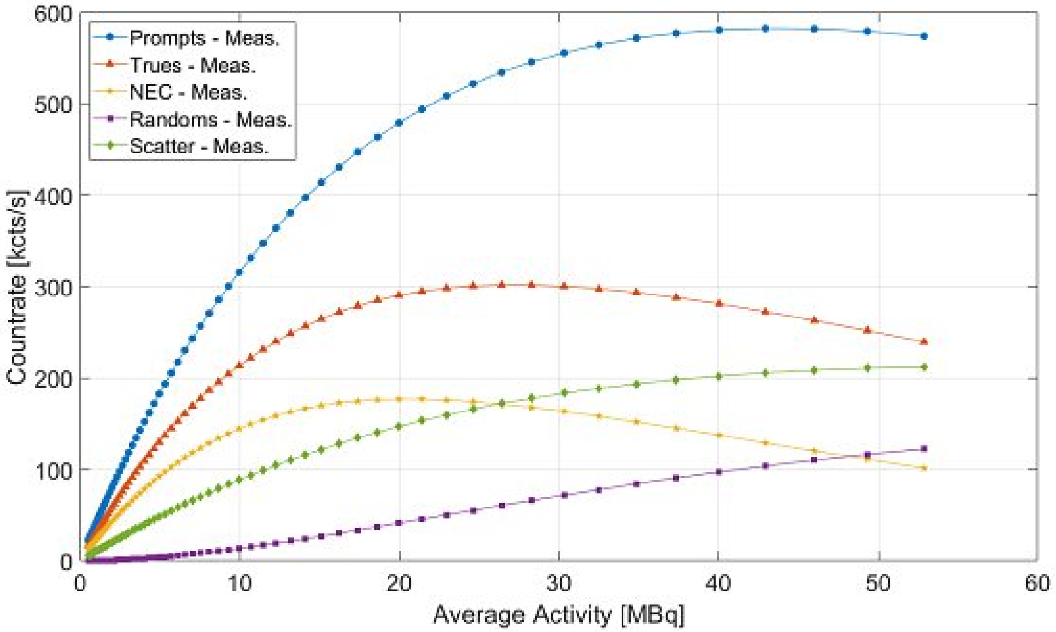

Figure 4.3: Measured countrates for rat-sized cylinder phantom – In the rat - sized cylinder, the peak NEC count rate reaches a maximum of 177 kcps at 21.4 MBq, whereas the peak true event count rate had its maximum value of 302 kcps at 28.3 MBq.

4.1.3 Spatial Resolution

At the axial center and 5 mm, 10 mm, 15 mm and 25 mm radial distance results for spatial resolution averaged over x, y, and z-direction were 1.55 mm, 2.29 mm, 2.29 mm and 1.0 mm FWHM, respectively. For the same transaxial locations but at $\frac{1}{4}$ of FOV axial distance from center, the measured values for spatial resolution were 1.47 mm, 1.62 mm, 1.62 mm and 1.71 mm FWHM, respectively. All values can be found in tables 4.1 and 4.2. With all values, visualized in figure 4.4 together with the results received for simulated measurements, the spatial resolution, averaged over x-, y- and z-direction measures 1.79 mm

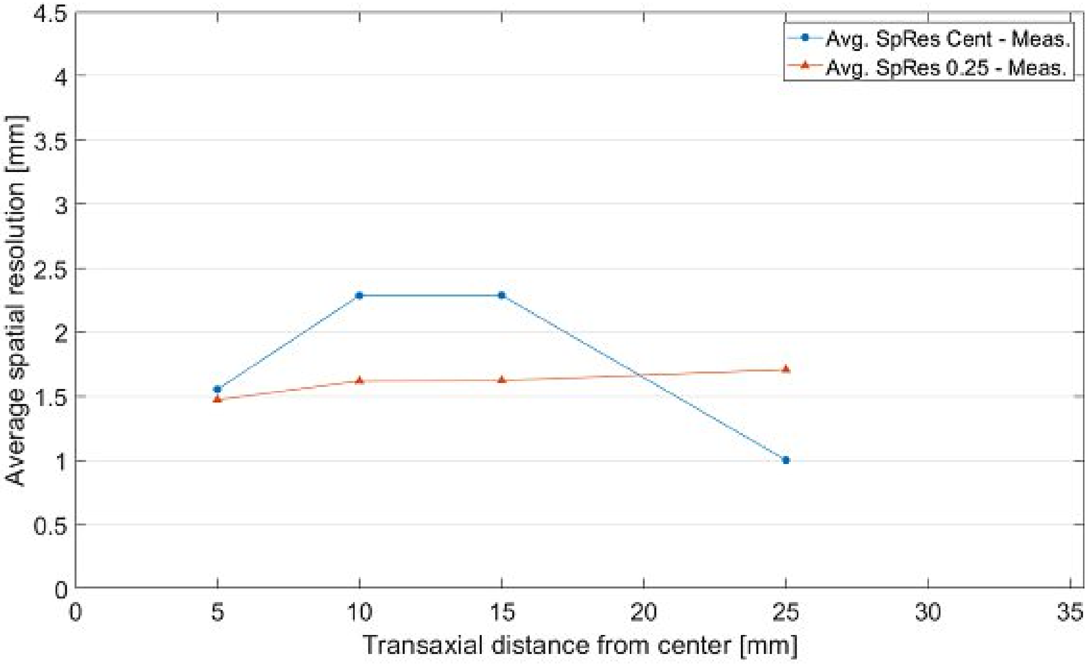

Figure 4.4: Results for spatial resolution measurements – The average spatial resolution increases towards the transaxial edges of the field of view for the measurement in the axial center (circular marks). A measurement outlier at the very edge of the field of view can be seen, which is most likely caused by incorrect source placement. For the measurement at $\frac{1}{4}$ of FOV axial distance from center, the spatial resolution is more stable with transaxial distance from center (triangular marks).

Reconstructed image pixel size: 0.25 mm × 0.25 mm								
Slice thickness: 1 mm								
At axial center								
transax. dist. [mm]	5		10		15		25	
	FWHM [mm]	FWTM [mm]	FWHM [mm]	FWTM [mm]	FWHM [mm]	FWTM [mm]	FWHM [mm]	FWTM [mm]
X	0.72	0.97	0.85	1.15	0.90	1.21	0.58	0.77
Y	0.87	1.17	1.00	1.34	1.03	1.39	0.35	0.46
Z	3.07	4.11	5.01	6.72	4.93	6.61	2.09	2.80
Volume [mm3̂]	1.93	4.66	4.26	10.30	4.60	11.12	0.42	1.00
Avg [mm]	1.55	2.08	2.29	3.07	2.29	3.07	1.00	1.35

Table 4.1: Results for spatial resolution at axial center of field of view

Reconstructed image pixel size: 0.25 mm × 0.25 mm								
Slice thickness: 1 mm								
At 1/4 of FOV								
transax. dist. [mm]	5		10		15		25	
	FWHM [mm]	FWTM [mm]	FWHM [mm]	FWTM [mm]	FWHM [mm]	FWTM [mm]	FWHM [mm]	FWTM [mm]
X	0.76	1.01	0.97	1.30	0.95	1.27	1.09	1.46
Y	0.79	1.06	0.78	1.04	0.78	1.05	0.62	0.83
Z	2.88	3.86	3.11	4.18	3.15	4.22	3.42	4.59
Volume [mm3̂]	1.71	4.14	2.34	5.66	2.32	5.61	2.29	5.53
Avg [mm]	1.47	1.98	1.62	2.17	1.62	2.18	1.71	2.29

Table 4.2: Results for spatial resolution at $\frac{1}{4}$ of field of view

4.1.4 Image Quality

In reconstructed images, voxels usually contain an activity per voxel volume, meaning an activity concentration, which is given in $\mathrm{kBq\,mL^{-1}}$. As the scanner investigated was still in a prototype stage, no absolute quantification was possible at the time of measurements due to the lack of necessary corrections implemented in the reconstruction algorithm. Therefore, mean, maximum and minimum uniformity are given in unitless numbers and all other results are relating to those absolute values.

The mean value calculated in the uniform region is 162.55 with a maximum of 257.18, a minimum of 91.08 and a relative standard deviation of 18.98 %. All values are given in table 4.3. Recovery coefficients for the 1 mm, 2 mm, 3 mm, 4 mm and 5 mm rods yield 0.08, 0.38, 0.83, 1.11 and 1.25, respectively. Standard deviations were 36 %, 23 %, 21 %, 20 % and 20 %, respectively. Table 4.4 summarizes all values as proposed by NEMA and they are given as a function of rod diameter in figure 4.5. Spill over ratios were 2.12 with a standard deviation of 34.71 % for the water filled cylinder and 1.00 with a standard deviation of 29.04 % for the cylinder filled with air. Values can be found in table 4.5.

	Mean	**Maximum**	**Minimum**	**STD**	**%STD**
Uniformity	162.55	257.18	91.08	30.85	18.98

Table 4.3: Results for uniformity test in Image Quality Phantom

Rod Diameter	**1 mm**	**% STD**	**2 mm**	**% STD**	**3 mm**	**% STD**	**4 mm**	**% STD**	**5 mm**	**% STD**
Recovery Coefficient	0.08	36.09	0.38	23.14	0.83	20.58	1.11	20.13	1.25	19.53

Table 4.4: Results for recovery coefficients depending on rod diameter

Region	**SOR**	**%STD**
Water-filled cylinder	0.12	34.71
Air-filled cylinder	0.06	29.04

Table 4.5: Results for accuracy of corrections

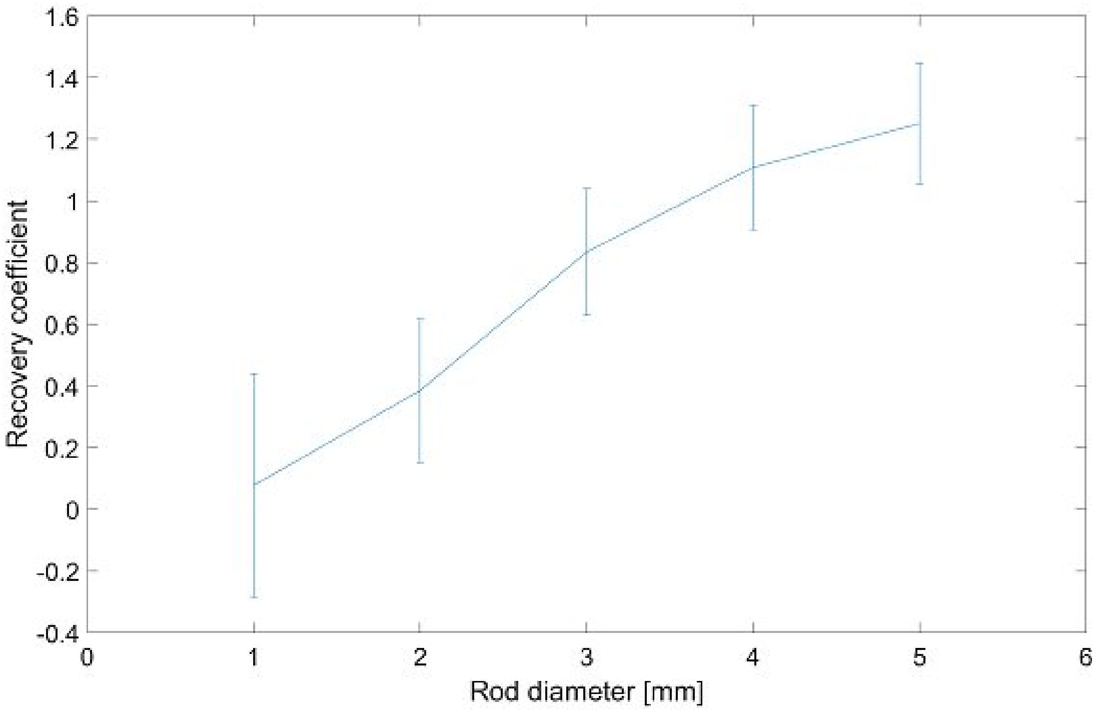

Figure 4.5: Results for recovery coefficients as a function of rod diameter – The recovery coefficients are plotted over the rod diameter, the error bars representing the respective standard deviations. The coefficients increase with rising rod diameter while the standard deviation slightly decreases.

4.2 Monte Carlo - Simulations

4.2.1 Sensitivity

As background count rates for absolute sensitivity were not taken into account for evaluations on the real scanner, they weren't considered for simulated values either.

For both GATE settings, absolute scanner sensitivity was highest at the axial and transaxial center of the FOV and decreased towards its edges. Curves for both settings were continuous except for the axial center. Maximum absolute sensitivity was 5.69 % for lower amount of Lutetium and Yttrium (Settings A) while it reached 6.95 % for a higher amount of the elements in the simulations (Settings B). The total absolute scanner sensitivity obtained for simulation type A was 3.55 % and 4.35 % for simulation type B. Both curves can be seen in figure 4.6 together with results for measured absolute scanner sensitivity.

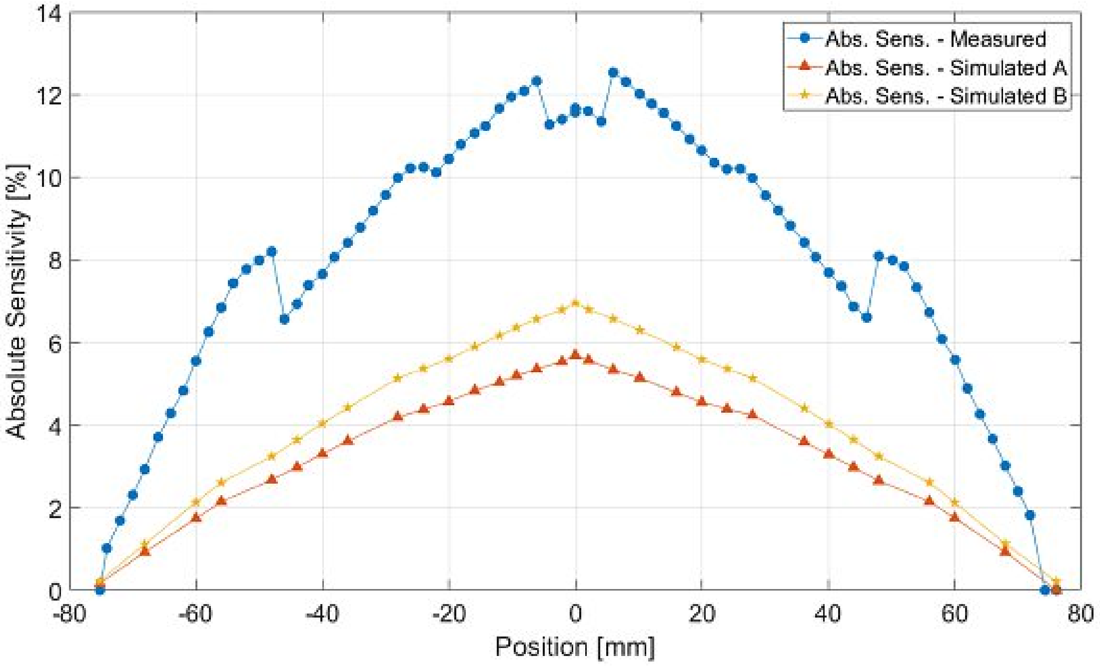

Figure 4.6: Comparison of Measured vs. simulated count rates for Sensitivity, both GATE settings – For GATE-simulations, sensitivity measurements rise continuously towards the center of the FOV for both settings which is in contrast to the measurements on the real scanner. Simulation settings A lead to a maximum sensitivity of 5.69 %, while simulation settings B result in a maximum scanner sensitivity of 6.95 %. It can be seen, that both simulations result in lower scanner sensitivity than real measurements.

4.2.2 Noise Equivalent Count Rate

Once again, no background count rates were considered for NEC-calculations on simulated data as they hadn't been taken into account for the real measurements. For simulation settings A, the mouse sized cylinder yielded its peak true count rate at 30.6 MBq reaching a value of 418 kcps while the NEC count rate had a maximum of 314 kcps at 26.6 MBq. For the bigger rat-sized phantom, true count rate had its maximal value of 320 kcps at 30.3 MBq while the NEC-count rate had a peak at 26.4 MBq and was 184 kcps. Values for all simulated activities, simulation type A, are depicted in figure 4.7 for the mouse cylinder and in figure 4.8 for the rat-like phantom. Both graphs include measured values on the real scanner.

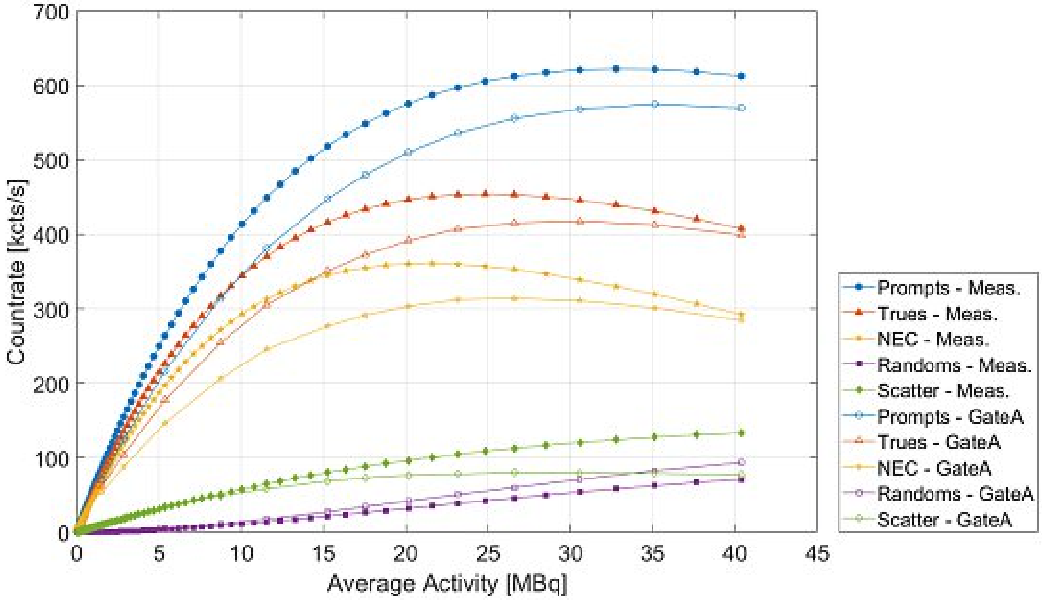

Figure 4.7: Comparison of measured vs. simulated count rates for mouse phantom, settings A – While the peak NEC count rate of 314 kcps was reached at 26.6 MBq, the maximum true count rate of 418 kcps was determined at 30.6 MBq for the simulated model. It can be seen, that for the mouse sized phantom, the true- and NEC-count rate in the GATE model are below the values for the measurements for all activities.

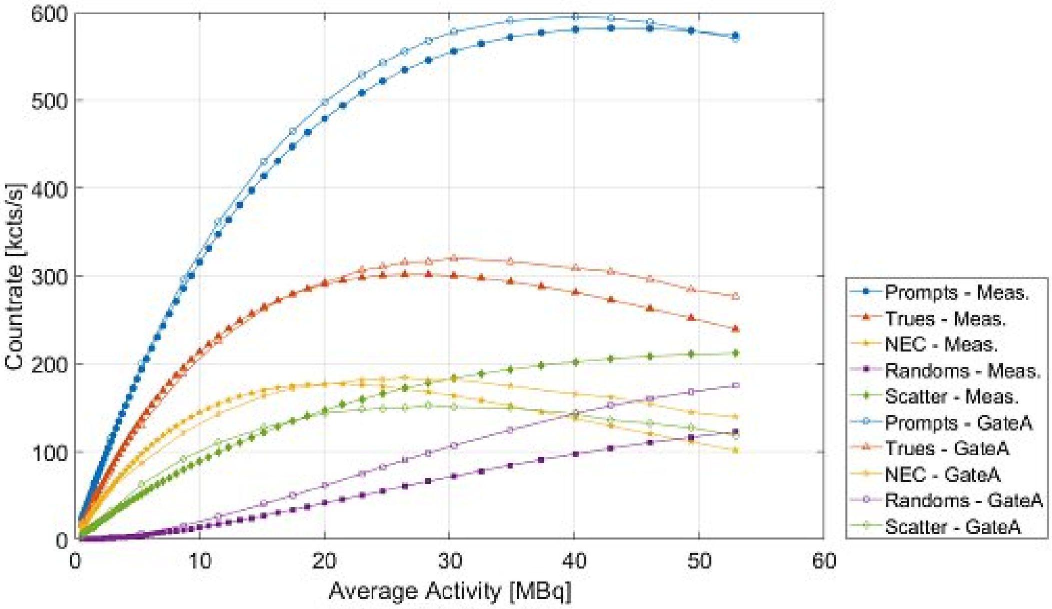

Figure 4.8: Comparison of measured vs. simulated count rates for rat phantom, settings A – The peak NEC count rate in the rat sized phantom was 184 kcps at 26.4 MBq, whereas the true count rate had its maximal value of 320 kcps at 30.3 MBq. In the rat-sized phantom, the simulated and measured prompt count rate show similar behavior while the peaks for the other count rates are shifted.

Simulation settings B lead to a peak of 523 kcps in true and of 440 kcps in NEC count rate, both values were reached at 30.6 MBq in the mouse-sized cylinder. In the rat-sized cylinder, the maximum true count rate was 487 kcps while the maximum NEC count rate was 370 kcps, both peaks appearing at an activity of 34.9 MBq. The results for all simulated NEC-measuremets with GATE settings B can be seen in figure 4.9 for the mouse-like cylinder and in figure 4.10 for the rat-sized phantom.

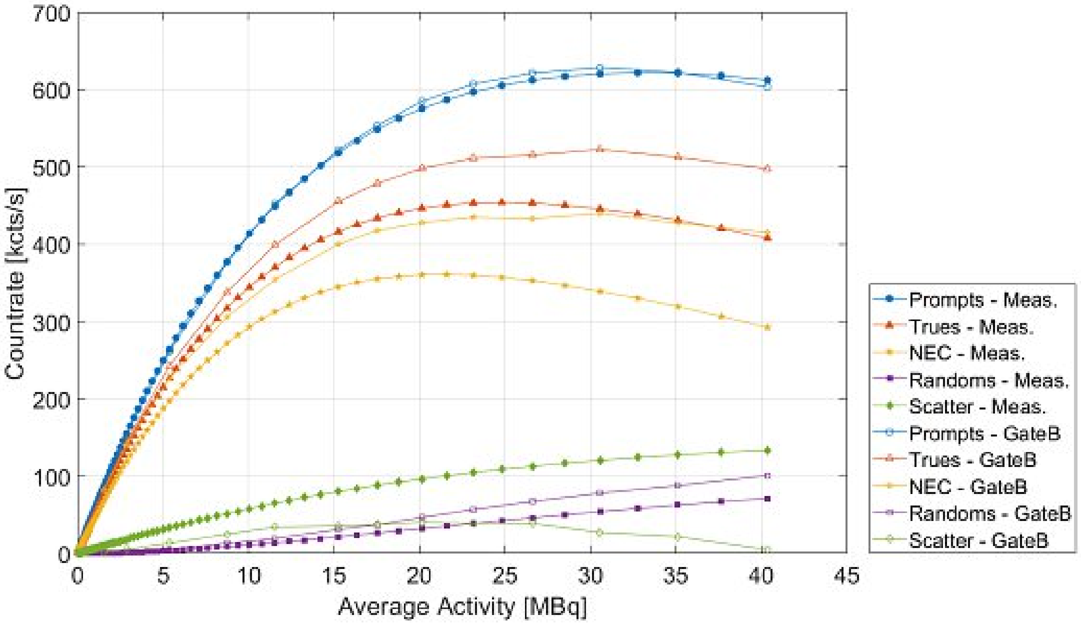

Figure 4.9: Comparison of measured vs. simulated count rates for mouse phantom, settings B – For simulation scenario B, in the mouse sized cylinder, a peak NEC count rate of 440 kcps and a maximum true count rate of 523 kcps was measured, both peaks occurring at 30.6 MBq. It is of note that the measured and simulated count rate are very similar while the count rates for scatter show diverging behavior.

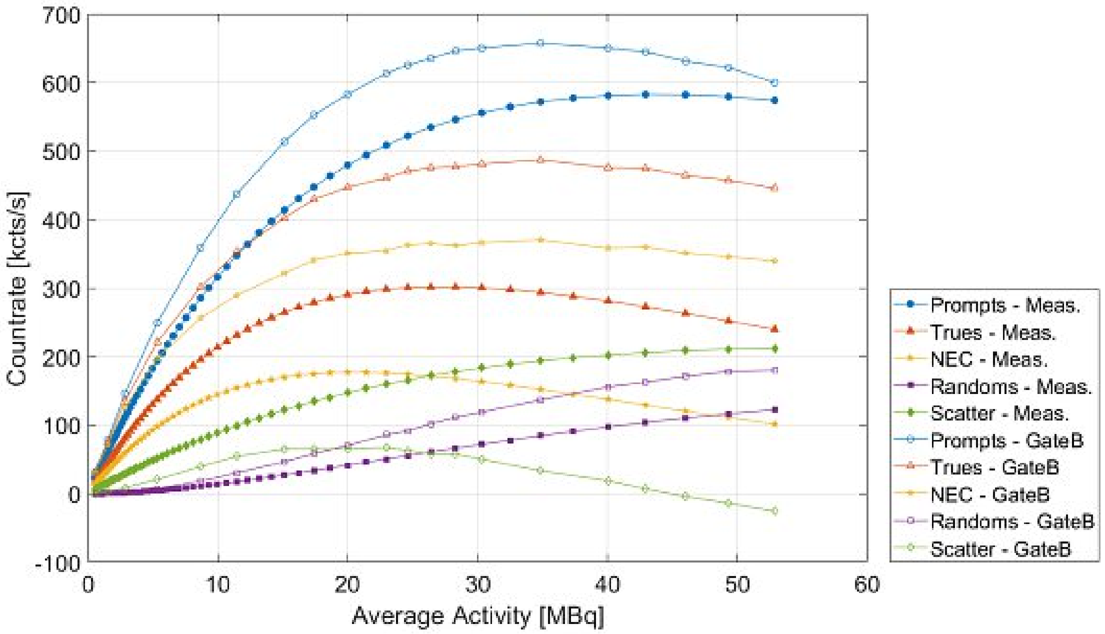

Figure 4.10: Comparison of measured vs. simulated count rates for rat phantom, settings B – The peak NEC count rate for the rat sized phantom and GATE settings B was 370 kcps and the true count rate reached a maximum of 487 kcps, both peaks occurring at an activity of 34.9 MBq. It is of note that simulated prompt, true, random and scatter count rates are above their measured pendents, while the simulated scatter count rate is lower than the measured values.

4.2.3 Spatial Resolution

For the Monte Carlo simulations, spatial resolution was 1.78 mm, 1.61 mm, 1.51 mm and 2.28 mm FWHM at the axial center of FOV and 1.13 mm, 1.18 mm, 1.17 mm and 2.15 mm FWHM at 37.5 mm axial distance from center of FOV for the transaxial distances 5 mm, 10 mm, 15 mm and 25 mm and GATE-settings A with lower amount of Lutetium and Yttrium. This yields to an average spatial resolution of 1.60 mm, the average at axial center (1.79 mm) being higher than at $\frac{1}{4}$ FOV (1.41 mm). A graphical representation of those values can be found in figure 4.11 together with the data of the real measurements for direct comparison.

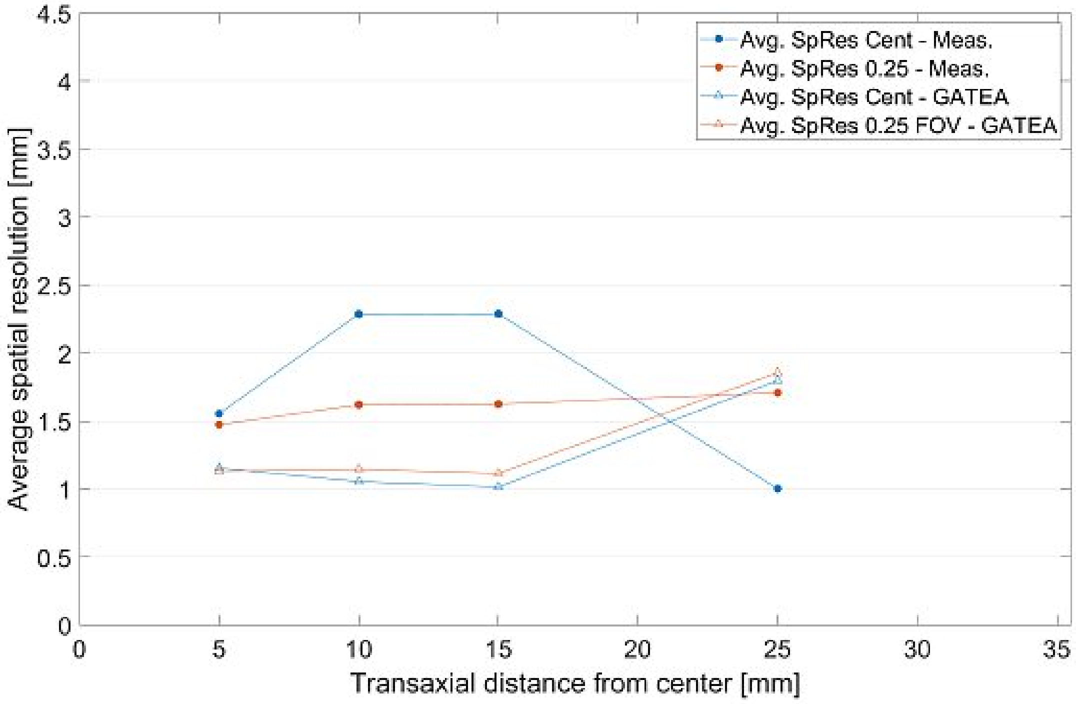

Figure 4.11: Spatial resolution results for measurements and simulation settings A, at both axial center as well as $\frac{1}{4}$ of field of view. – The model scanner's average spatial resolution is mostly stable for axial as well as transaxial distance from the origin with a sudden increase at the transaxial edge of the FOV. The simulated average spatial resolution presents itself generally lower than the measured one.

For GATE-settings B, where Lutetium and Yttrium were present in higher concentrations, spatial resolution was 1.12 mm, 1.02 mm, 0.98 mm and 1.44 mm FWHM at the axial center of FOV and 0.69 mm, 0.74 mm, 0.73 mm and 0.72 mm FWHM at $\frac{1}{4}$ of FOV for the transaxial distances 5 mm, 10 mm, 15 mm and 25 mm, respectively. Thus, an average scanner spatial resolution of 0.93 mm is calculated, with the average at axial center (1.14 mm) being higher than at $\frac{1}{4}$ of FOV (0.72 mm). Values are depicted in figure 4.12 along with obtained values from the real measurements.

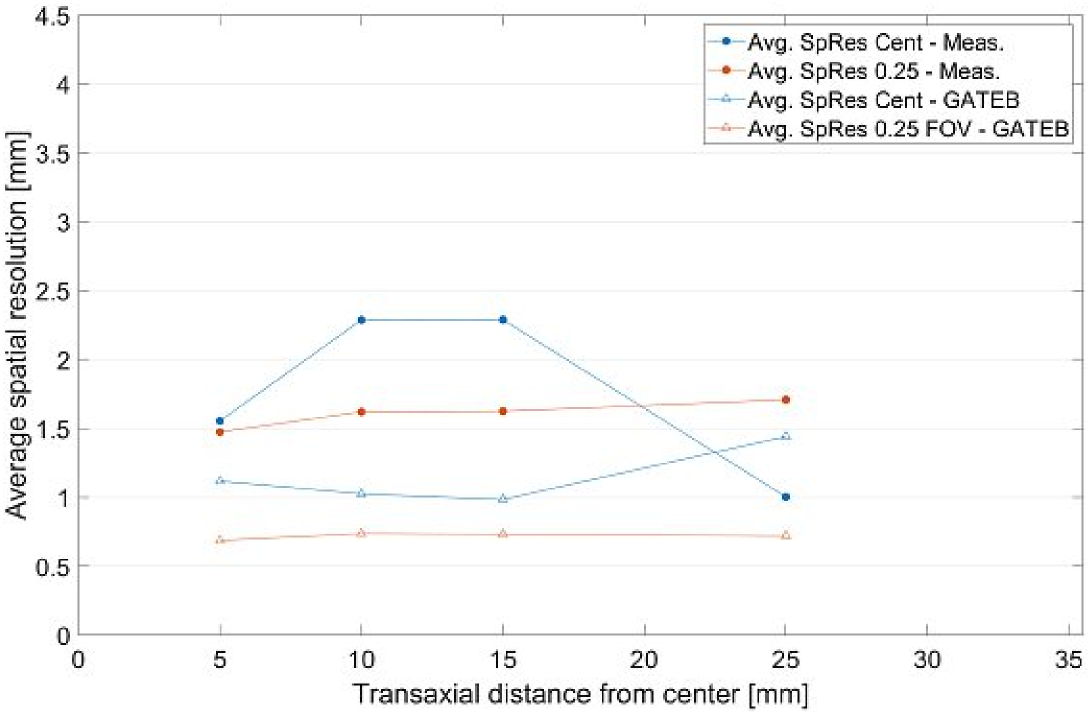

Figure 4.12: Spatial resolution results for measurements and simulation settings B, at both axial center as well as $\frac{1}{4}$ of field of view. – At $\frac{1}{4}$ of field of view the model scanner's average spatial resolution is better and more stable than at the center of the scanner, where the spatial resolution rises towards the edge of the transaxial field of view.

5. Discussion

The performance of the preclinical PET Insert ”Si 198” was evaluated. The scanner was simulated and performance measurements were reproduced using a Monte Carlo simulation software.

5.1 Performance Measurements on the PET Insert

Sensitivity While the maximum sensitivity of 12.53 % was reached at 6 mm distance from center for measurements, the obtained value for the central position was 11.67 %, which is comparable to reported values at the same position (11 %, [42]). At 40 mm distance from center, results for absolute sensitivity are slightly below 8 %, which is higher than reported (6.6 %). A possible explanation for measuring lower sensitivity in [42] could be their correction for intrinsic scintillator radioactivity, which wasn't performed within this project. To correct for intrinsic detector activity, a background scan has to be performed, which is an acquisition without a source present in the FOV. The counts detected in this acquisition are postulated to originate from the detector itself. This is, because the deployed material, LYSO, contains the radioactive isotope ^{176}Lu. While 97.4 % of the naturally occurring element is ^{175}Lu, which is stable, also an unstable isotope is present. 2.6 % of Lutetium is ^{176}Lu, which itself decays via β^--radiation (values taken from [22]). Despite performing such scans, the intrinsic count rate couldn't be determined, as the obtained sinograms contained non-numerical values. This behavior indicates, that a common readout method employing memory buffers could be used. There, values are only written into raw-data files once a buffer is full. However, if no activity is present, the buffer won't fill in a reasonable time. As no background countrate could be determined, an overestimation of the count rate might have occurred.

While [42] report continuous scanner-sensitivity along the axial FOV, the graph in figure 4.6 clearly exhibits discontinuities. This could result from variations between the PET Inserts. While at MedUni Vienna, a 9.4 T MR surrounds the insert, it was testet in a 7 T magnetic field in [42]. Additionally, SW changes could influence results, as the scanner in Vienna was installed after the one in Leuven [42]. Variations in data processing could lead to different counting behavior. However, a this presumption could not be verified, as information is missing in [42] on the used SW version.

Also other groups have reported discontinuous sensitivity behavior for preclinical scanners [43]. [44] examined a dedicated brain-PET system utilizing monolythic crystals and resembling jumps were observed for sensitivity as in the study presented within this thesis. In both studies, jumps don't appear at positions where detector gaps occur, but rather in their central region.

The toothed curve in figure 4.1 could be a result of restricting certain LORs. For LORs between axially distant detector rings, the angle at which the photons hit the detector is very small, making an assessment of where exactly the photon interacted with the crystal very hard. To avoid this, the distance between rings detecting a coincidence pair can be restricted. Rings at the very edge of a scanner only have neighboring rings on one side, which means there are less LORs allowed for them than for rings further inside. However, this also applies to detector rings inside the scanner, if they are right next to a gap. This causes an overlay of multiple triangular sensitivity profiles along the z axis, resulting in jumps in the sensitivity profile.

Also count rate statistics could influence absolute sensitivity concerning total values and curve form. Count rate statistics itself is heavily influenced by acquisition time. For all performance measurements on the real PET Insert, acquisition times were set as stated in table 3.1, meaning 10 s were set for each sensitivity measurement. Nevertheless, the response of the vendor-supplied program to create sinograms displayed that the real acquisition times differed from the settings. As aforementioned software performs a time-related averaging of values (meaning sinograms contain count rates rather than total counts), this behavior was taken into account for the evaluation of all results. Nevertheless, as the actual acquisition time was below 5 s, negative effects on counting statistics could influence results.

Noise Equivalent Count Rate A comparison of reported measurements with obtained results for maximum NEC and true count rates using rat- and mouse-sized cylinder phantoms can be found in tables 5.1 and 5.2. Count rates observed within this project were 25 % to 28 % lower than reported by [42]. The activities, at which peak true and NEC count rates were measured, deviated by approximately −6 % from reported values [42] for both phantoms, with an outlier of −11.4 % for the activity of the maximum true-count rate in the mouse sized phantom. Furthermore, in [42], the random count rate exceeds the scatter count rate between 36 MBq to 37 MBq for the rat-sized phantom. Despite the initial activity used within this project being above that (53.04 MBq), no intersection was determined.

As photons having an energy which lies outside of the deployed energy window are dismissed, this setting has an influence on the number of detected photons and thus on count rates. Also the coincidence timing window used can have an impact on the results for count rates. However, a consistent comparison with literature was challenging, as details about energy window and coincidence timing window were not given in [42]. Within this project, NEC count rates were obtained with an energy window of 250 keV to 771 keV and a coincidence timing window of 7 ns.

Apart from that, the NEMA standard requires an intrinsic count rate correction, which in general is performed by subtracting the count rate of a background acquisition from relevant actual acquisitions. Despite having performed said background scans within this project, they could not be used for intrinsic count rate correction, as respective sinograms only contained non-numerical values. [42] performed background acquisitions, which could also be a reason for the differing results of count rate behavior.

	Mouse-phantom			
	true count rate		**NEC count rate**	
	Max. ctrate [kcts/sec]	Activity [MBq]	Max. ctrate [kcts/sec]	Activity [MBq]
Gsell 2020	628	28	486	23
Measured	454	24.81	361	21.60
deviation	-27.7%	-11.4%	-25.7%	-6.1%

Table 5.1: Comparison of NEC- and true count rate maxima for mouse-sized cylinder phantom of [42] and values obtained within this project.

	Rat-phantom			
	true count rate		**NEC count rate**	
	Max. ctrate [kcts/sec]	Activity [MBq]	Max. ctrate [kcts/sec]	Activity [MBq]
Gsell 2020	410	30	239	23
Measured	302	28.3	177	21.43
deviation	-26.3%	-5.7%	-25.9%	-6.8%

Table 5.2: Comparison of NEC- and true count rate maxima for rat-sized cylinder phantom of [42] and values obtained within this project.

Spatial Resolution Tables 4.1 and 4.2 show, that spatial resolution is worse along the z-axis than in the xy-plane. Within this thesis, pixel dimensions in axial direction exceed dimensions in transaxial directions. To achieve high spatial resolution, a sharp signal edge is necessary, which entails high frequencies for correct representation. The maximum measured signal frequency, however, is defined by the sampling frequency and thus influenced by the pixel size [45]. Conclusively, bigger pixel sizes result in worsened spatial resolution. Furthermore, the homogeneous magnetic field from the MR scanner surrounding the PET insert has an effect on the annihilation point of positrons. As positrons are charged particles, the B field pushes their annihilation points into a cigar like shape along the scanner axis. Therefore, the FWHM calculations may be influenced as the distribution of annihilation positions is not symmetrical.

An increase of values for FWHM with the radial distance from center can be observed, as was expected [46, 47]. Source misplacement is a plausible explanation for the measurement outlier at 25 mm radial discance, center of FOV: As the source was positioned outside of the FOV, a noise pixel was detected for fitting the FWHM by the automated algorithm for finding the maximum value. As a result, the value for FWHM at this position is much smaller than reasonable.

With the measurement outlier left aside, all other values are above or very close to 1.5 mm FWHM for all source positions using FBP reconstructed images, with an average scanner spatial resolution of 1.79 mm and results being better at $\frac{1}{4}$ of FOV than at the axial center of the scanner FOV. Those observations are much higher than what was observed by Gsell et al. Gsell et al. [42], who reported below 1 mm spatial resolution for all positions. It should be noted, however, that there, images were reconstructed using MLEM-reconstructions with 36 iterations. Iterative reconstruction algorithms usually lead to better spatial resolution than analytical methods, as more precise modeling of the system is possible [46, 48]. In addition, Gsell et al. [42] placed the insert inside a 7 T field, while for this project, the insert was placed inside a 9.4 T field. As described above, the magnetic field has an influence on the distribution of positron annihilation points, which could also be a reason for differences from measured to reported values.

Image Quality For the image quality phantom, recovery coefficients varying between 0.08 and 1.25 were obtained, all with an energy threshold of 250 keV. While [43] present similar values for smaller rod sizes, the decline of RCs above a certain rod-diameter couldn't be observed within this project. As Gsell et al. [42] only report the RC for the 3 mm rod, further comparison was unobtainable. Spill over ratios (SOR) for water and air of 0.12 and 0.06 respectively, appear better than the reported 0.21–0.23 [42] and 0.12, respectively. However, given the use of different reconstruciton algorithms and parameters, these deviations seem reasonable

5.2 Validation of the Monte Carlo Model

Sensitivity Both simulations result in lower scanner sensitivity than real measurements. The deviations of simulated to measured total scanner sensitivity are $\approx -55\,\%$ for GATE simulations type A and $\approx -45\,\%$ for simulations type B.

Lower sensitivity in the model compared to the measured values means, that fewer photons were detected in the model than during experiments. For photon detection, APDs show less gained signal per detected photon than SiPMs (see chapter 2.1.3). According to the GATE - user manual [49], the option "TakeEnergyCentroid" in the digitizer-module "readout" resembles SiPM rather than APD behavior. Some effort was put into simulating the readout with this option, but the simulation software didn't run with those settings. Hence, the option "TakeEnergyWinner" was used, imitating APD like signal gain. Less output could have an impact on counting statistics, resulting in less detected photons.

Similarly, the attempt to model crosstalk effects between crystals was not successful. This was desirable because the monolythic crystals, as applied in the real scanner, were simulated as "real" pixels to match the virtual pixels and to be able to create sinograms. As the simulated pixels are physically distinct, crosstalk simulation might have an impact on measured sensitivity.

The differing results for varying crystal compositions suggest, that the detector constitution has an impact on sensitivity. [7] created a GATE model for a prototype preclinical PET scanner and it was found, that the LYSO utilized in the system they modeled has different stopping power than the LYSO defined in the pre-defined GATE library. Therefore, a customized LYSO mix was used in their simulations. For the GATE simulations performed within this project, the density of LYSO was also adapted to a commonly found value of $7.3\,\mathrm{g\,cm^{-3}}$. Nonetheless, as exact detector material composition was not disclosed, a more precise simulation couldn't be implemented, which could lead to deviations from measured to simulated values.

Though assumptions outlined above can be made, it remains unclear, why simulation results differ from measured values. Even more so, as there are examples in literature, where simulated sensitivity exceeds measured results. Due to incomplete explanations and descriptions of methods, however, it is challenging to compare values, as is explained in the following example: Zeraatkar et al. [50] created the Monte Carlo model of a small animal scanner employing pixelated BGO crystals and compared it to the real system. They reported a sensitivity of 11.2 % at an energy threshold of 300 keV for the Monte Carlo model, which was about ≈25 % higher than for the real scanner. Their method, however, was to use a custom-made sensitivity source of a ^{22}Na point source surrounded by Aluminium as opposed to acrylic glass, which is NEMA standard. Then, a scaling factor was calculated from the deviation and applied to all other measurements. Subsequently, sensitivity measurements using the NEMA-source were simulated with an energy threshold of 340 keV, for which the scanner shows a sensitivity of only 4.2 %. While it wasn't clearly stated, if the same scaling factor was applied for those simulations, additionally, the NEMA-simulations were not compared to real measurements. Furthermore, energy windows varied for the sensitivity measurements, making it hard to assess the model's behavior for NEMA-standard measurements.

Noise Equivalent Count Rate Also for NEC measurements, both GATE settings were compared. For the mouse-sized phantom, the maximum true count rate for GATE settings A is 8 % lower than measured, with the activity at which the peak occurs being 23 % higher. For settings B, the true count rate peak also occurs at a 23 % shift in activity, however resulting in a 15 % higher true count rate than measured. In the NEC count rate, GATE settings A led to a peak 13 % lower than measured, appearing at a 23 % higher activity than the measured peak count rate. For GATE settings B, the peak NEC count rate exceeded the measured values by 22 %, ocurring at an activity shifted by 42 %. Judging by prompt count rate in the mouse sized phantom only, model B reproduces the scanner behavior better than model A. It stands out that for model B, all peak count rates occur at the same activity of 30.56 MBq. An overview of all values obtained with the mouse-sized cylinder is given in table 5.3.

	Mouse-phantom					
	prompt count rate		**true count rate**		**NEC count rate**	
	Max. ctrate [kcts/sec]	Activity [MBq]	Max. ctrate [kcts/sec]	Activity [MBq]	Max. ctrate [kcts/sec]	Activity [MBq]
Measured	622	32.76	454	24.81	361	21.60
GATE A	575	35.12	418	30.56	314	26.60
deviation	-7.6%	7.2%	-7.9%	23.2%	-13.0%	23.1%
GATE B	628	30.56	523	30.56	440	30.56
deviation	1.0%	-6.7%	15.2%	23.2%	21.9%	41.5%

Table 5.3: Comparison of NEC- and true count rate maxima for mouse-sized cylinder phantom of measured values and values obtained from Monte Carlo simulations.

In the rat sized cylinder, count rate deviations are below 10 % for GATE settings A, while the activity at which peak count rates occur differs between −6 % to 23 %. For GATE settings B, however, count rates vary up to 109 % and respective activities between −19 % to 63 %. For the rat cylinder, too, all count rate peaks in GATE model B appear at the same activity, here at 34.85 MBq. An overview of all values obtained with the rat-sized cylinder is given in table 5.4.

	Rat-phantom					
	prompt count rate		**true count rate**		**NEC count rate**	
	Max. ctrate [kcts/sec]	Activity [MBq]	Max. ctrate [kcts/sec]	Activity [MBq]	Max. ctrate [kcts/sec]	Activity [MBq]
Measured	582	42.93	302	28.30	177	21.43
GATE A	595	40.05	320	30.33	184	26.40
deviation	2.2%	-6.7%	6.0%	7.2%	4.0%	23.2%
GATE B	657	34.85	487	34.85	370	34.85
deviation	12.9%	-18.8%	61.3%	23.1%	109.0%	62.6%

Table 5.4: Comparison of NEC- and true count rate maxima for rat-sized cylinder phantom of measured values and values obtained from Monte Carlo simulations.

The prompt count rates for the simulations fit within a reasonable difference. With variations of up to 10 % being acceptable for simulations of real systems, true and NEC countrates are quite far away. The model's countrate behavior could be influenced by the selection of readout parameters, corresponding to sensitivity measurements. The choice "TakeEnergyWinner" in the digitizer module "readout" resembles APDs more than SiPMs. As explained, the gain of SiPMs is higher (section 2.1.3), which can have an impact on the count rates detected. It also applies to count rate behavior, that the lack of simulating crosstalk effects could have an influence on results. As the crystal has to be simulated as pixelated to extract sinograms, the model implies a physical distance between crystals.

As can be seen in figures 4.8 and 4.10, especially simulated scatter count rates deviate from the real measurements. As the necessary information was not retractable from specification sheets provided by the vendor, the Monte Carlo simulated model was created without plastic housing holding the detector rings in place. It can be assumed that a model including more scanner framework would mimic the scatter count rates more accurate.

A very simulation specific setting could be another reason for modeled count rates differing from real ones. In GATE, a so called energy cut has to be selected for all types of particles involved, for each volume where they appear. This energy cut determines the threshold, below which no secondary particles are generated. [51] investigated the influence of said photon energy cut on count rates for scatter, random and true coincidences. There, an abrupt rise of count rates vs. photon energy cut at approximately 10 keV was reported.

At this point it should be mentioned, that the differences between measured and simulated data should be taken with a grain of salt. Different systems may behave differently depending on variations in the quality of individual parts. This is well demonstrated in [11], where a GATE model of a clinical scanner was created. Subsequently, the simulated countrate measurements were not only compared to one, but two installed systems of the same clinical scanner. There, the modeled countrates lay between measured ones.

Furthermore, in [39] a Monte Carlo model for another clinical scanner which is specifically used for brain imaging was created. With smaller detector distance than conventional clinical scanners, those systems have a lot in common with preclinical scanners. This group reported the simulated peak count rates occurring at the same activity concentrations as the measured ones. As for other methods cited above, comparison was difficult, as a very sparse simulation of 5 datapoints was carried out. Additionally, the NEMA standard for clinical scanners was used, which differs from the preclinical standard.

Spatial Resolution For GATE-settings A, where LYSO with lower Lutetium-Yttrium concentration is simulated, an average over transaxial positions shows better spatial resolution at axial center than at $\frac{1}{4}$ of FOV. Furthermore, an increase towards the transaxial edge of FOV could also be observed in simulations, compliant with [47].

GATE-Settings B meet the real measurements better than A in the respect, that here, average spatial resolution is better at $\frac{1}{4}$ of FOV than at the axial center. Additionally, it can be observed that GATE model B maps real measurements better regarding transaxial variation at $\frac{1}{4}$ of FOV, as there are hardly any variations for the spatial resolutions.

Comparing the average real scanner spatial resolution of 1.79 mm to the simulated values, however, detector composition A yields in results (1.60 mm) closer to reality than composition B (0.93 mm).

For simulations type B, a higher proportion of Lutetium and Yttrium was simulated than for A, which means that photons have more interaction partners in the detector. Therefore, the mean free path of photons is shorter, which results in scintillation points closer to the surface. The distance between actual scintillation point and detector surface is called depth of interaction (DOI). If it is not measured in a scanner, the detector surface is determined as the scintillation point. Hence, the closer the true scintillation point is to the detector surface, the smaller the deviation of assigned LOR to the real LOR. This could explain, why results for spatial resolution are better in simulations type B.

Aside from uncertainties originating from the simulation model itself, also sinogram extraction was not straightforward for simulated data. The documentation provided for the applied software, "OMEGA", was not complete. For instance, arc correction couldn't be computed automatically. Especially for LORs at large transaxial distances from center, arc correction has a high impact, as the potential LORs have smaller distances as in the center.

6. Conclusion

Performance measurements based on the NEMA NU4-2008 standard were carried out at the preclinical PET Insert "Si 198", manufactured by Bruker BioSpin GmbH. An overall scanner sensitivity of 7.95 % was determined. Peak NEC count rates of 177 kcps at 21.4 MBq for the rat sized cylinder and 361 kcps at 21.6 MBq were measured. An average scanner spatial resolution of 1.79 mm was obtained.

Furthermore, a Monte Carlo simulated model of said scanner was created. While results for prompt countrate simulations show deviations of below or slightly above 10 % from the real measurement, scatter behavior differs clearly and depends on the phantom used for measurements as well as crystal composition applied.

Sensitivity performance could be recreated in its basic sense, meaning that, sensitivity in general is best at the center of the FOV and decreases towards the edges. Although this was the case, scanner sensitivity is poorly represented by the simulation model. Depending on the element ratio in the detector material, deviations from simulated to measured data were between 45 % to 55 %.

Spatial resolution is modeled fairly acceptable. Also for this type of measurements, the detector composition has an influence on the results, leading to an average spatial resolution of 1.6 mm and 0.93 mm for simulations A and B, respectively.

This indicates that the model needs adjustments of parameters such as the exact scintillator crystal composition. Moreover, including the detector housing in the simulation could significantly improve scatter behavior. Additionally, the model could benefit from more realistic readout electronics simulation. This type of information could significantly improve the simulation model's applicability. At the same time such details could be difficult to obtain from the vendor as they are most likely undisclosed. Also the current GATE implementation could have an impact on the model's accuracy. The employed version might not be optimal to model a monolythic crystal system. With improvements in future SW versions, this feature could be upgraded. Consequently, crosstalk effects and readout performance could significantly improve the simulation model's accuracy.

Bibliography

[1] T. Beyer et al. "A combined PET/CT scanner for clinical oncology." In: *Journal of nuclear medicine : official publication, Society of Nuclear Medicine* 41 (8 Aug. 2000), pp. 1369–1379. ISSN: 0161-5505. ppublish.

[2] Ciprian Catana et al. "Simultaneous acquisition of multislice PET and MR images: initial results with a MR-compatible PET scanner." In: *Journal of nuclear medicine : official publication, Society of Nuclear Medicine* 47 (12 Dec. 2006), pp. 1968–1976. ISSN: 0161-5505. ppublish.

[3] Claudia Kuntner and David Stout. "Quantitative preclinical PET imaging: opportunities and challenges". In: *Frontiers in Physics* 2 (2014). DOI: `10.3389/fphy.2014.00012`.

[4] Miles Wernick and John Aarsvold. *Emission Tomography*. Elsevier, 2004.

[5] S Jan et al. "GATE: a simulation toolkit for PET and SPECT". In: *Physics in Medicine and Biology* 49.19 (Sept. 2004), pp. 4543–4561. DOI: `10.1088/0031-9155/49/19/007`.

[6] S. Agostinelli et al. "Geant4—a simulation toolkit". In: *Nuclear Instruments and Methods in Physics Research Section A: Accelerators, Spectrometers, Detectors and Associated Equipment* 506.3 (July 2003), pp. 250–303. DOI: `10.1016/s0168-9002(03)01368-8`.

[7] G. Stortz et al. "Characterization of a New MR Compatible Small Animal PET Scanner Using Monte-Carlo Simulations". In: *IEEE Transactions on Nuclear Science* 60.3 (June 2013), pp. 1637–1644. DOI: `10.1109/tns.2013.2256927`.

[8] Antonio J. Gonzalez et al. "Feasibility Study of a Small Animal PET Insert Based on a Single LYSO Monolithic Tube". In: *Frontiers in Medicine* 5 (Nov. 2018). DOI: `10.3389/fmed.2018.00328`.

[9] M. Ljungberg, S.E. Strand, and M.A. King. *Monte Carlo Calculations in Nuclear Medicine: Applications in Diagnostic Imaging*. Series in Medical Physics and Biomedical Engineering. CRC Press, 2012. ISBN: 9781439841105. URL: `https://books.google.at/books?id=YzzNBQAAQBAJ`.

[10] B Aklan et al. "GATE Monte Carlo simulations for variations of an integrated PET/MR hybrid imaging system based on the Biograph mMR model". In: *Physics in Medicine and Biology* 60.12 (June 2015), pp. 4731–4752. DOI: `10.1088/0031-9155/60/12/4731`.

[11] C. Ross Schmidtlein et al. "Validation of GATE Monte Carlo simulations of the GE Advance/Discovery LS PET scanners". In: *Medical Physics* 33.1 (Dec. 2005), pp. 198–208. DOI: `10.1118/1.2089447`.

[12] P. Hendrik Pretorius et al. "A mathematical model of motion of the heart for use in generating source and attenuation maps for simulating emission imaging". In: *Medical Physics* 26.11 (Nov. 1999), pp. 2323–2332. DOI: `10.1118/1.598746`.

[13] W.P. Segars, D.S. Lalush, and B.M.W. Tsui. "Modeling respiratory mechanics in the MCAT and spline-based MCAT phantoms". In: *IEEE Transactions on Nuclear Science* 48.1 (2001), pp. 89–97. DOI: `10.1109/23.910837`.

[14] NEMA. *About the National Electrical Manufacturers Association*. 2020. URL: `https://www.nema.org/about` (visited on 12/06/2020).

[15] NEMA. *NEMA NU 4 - 2008 Performance Measurements of Small Animal Positron Emission Tomographs*. Tech. rep. Rosslyn, VA: National Electrical Manufacturers Association, 2008.

[16] Antonio Gonzalez Martinez et al. "A PET design based on SiPM and monolithic LYSO crystals: Performance evaluation". In: *IEEE Transactions on Nuclear Science* 63 (June 2016), pp. 1–7. DOI: `10.1109/TNS.2016.2522179`.

[17] Dale L. Bailey and David W. Townsend. *Positron Emission Tomography - Basic Sciences*. Springer, 2005.

[18] Jacobo Cal-Gonzalez et al. "Hybrid Imaging: Instrumentation and Data Processing". In: *Frontiers in Physics* 6 (2018), p. 47. ISSN: 2296-424X. DOI: `10.3389/fphy.2018.00047`. URL: `https://www.frontiersin.org/article/10.3389/fphy.2018.00047`.

[19] G. Hevesy. "The Absorption and Translocation of Lead by Plants: A Contribution to the Application of the Method of Radioactive Indicators in the Investigation of the Change of Substance in Plants." In: *The Biochemical journal* 17 (4-5 1923), pp. 439–445. ISSN: 0264-6021. DOI: `10.1042/bj0170439`. ppublish.

[20] Jens Maus. "Event-Driven Motion Compensation in Positron Emission Tomography: Development of a Clinically Applicable Method". PhD thesis. Technische Universität Dresden, Dresden, 2009.

[21] Simon Cherry, James Sorenson, and Michael Phelps. *Physics in Nuclear Medicine*. Saunders Elsevier, 2012.

[22] NNDC, Brookhaven National Laboratory. *NuDat - Interactive Chart of Nuclides*. URL: `https://www.nndc.bnl.gov/nudat2/chartNuc.jsp` (visited on 02/14/2021).

[23] National High Magnetic Field Laboratory. *Molecular Expressions*. URL: `https://micro.magnet.fsu.edu/primer/digitalimaging/concepts/photomultipliers.html` (visited on 03/09/2021).

[24] Fabio Acerbi and Stefan Gundacker. "Understanding and simulating SiPMs". In: *Nuclear Instruments and Methods in Physics Research Section A: Accelerators, Spectrometers, Detectors and Associated Equipment* 926 (May 2019), pp. 16–35. DOI: `10.1016/j.nima.2018.11.118`.

[25] CAEN Group. *Electronics for Silicon Photomultipliers*. URL: `https://www.caen.it/subfamilies/electronics-for-silicon-photomultipliers/` (visited on 03/12/2021).

[26] Mónica Vieira Martins. "Positron Emission Mammography". In: *Mammography Techniques and Review*. InTech, July 2015. DOI: `10.5772/60452`.

[27] RD Badawi. *Introduction to PET physics*. 1999. URL: `https://depts.washington.edu/imreslab/from%20old%20SITE/pet_intro/` (visited on 03/10/2021).

[28] M. E. Daube-Witherspoon and G. Muehllehner. "Treatment of axial data in three-dimensional PET." In: *Journal of nuclear medicine : official publication, Society of Nuclear Medicine* 28 (11 Nov. 1987), pp. 1717–1724. ISSN: 0161-5505. ppublish.

[29] L. A. Shepp and Y. Vardi. "Maximum Likelihood Reconstruction for Emission Tomography". In: *IEEE Transactions on Medical Imaging* 1.2 (Oct. 1982), pp. 113–122. DOI: `10.1109/tmi.1982.4307558`.

[30] H.M. Hudson and R.S. Larkin. "Accelerated image reconstruction using ordered subsets of projection data". In: *IEEE Transactions on Medical Imaging* 13.4 (1994), pp. 601–609. DOI: `10.1109/42.363108`.

[31] Shan Tong, Adam M. Alessio, and Paul E. Kinahan. "Image reconstruction for PET/CT scanners: past achievements and future challenges." In: *Imaging in medicine* 2 (5 Oct. 2010), pp. 529–545. ISSN: 1755-5191. DOI: `10.2217/iim.10.49`. ppublish.

[32] Frederic H Fahey. "Data acquisition in PET imaging". In: *Journal of nuclear medicine technology* 30.2 (June 2002), pp. 39–49. ISSN: 0091-4916. URL: `http://tech.snmjournals.org/cgi/content/full/30/2/39`.

[33] Nicholas Metropolis et al. "Equation of State Calculations by Fast Computing Machines". In: *The Journal of Chemical Physics* 21.6 (June 1953), pp. 1087–1092. DOI: `10.1063/1.1699114`.

[34] Brown Dwarfs in New York City. *Brown Dwarf Research at AMNH, Hunter College-CUNY, and Macaulay Honors College-CUNY.* URL: `http://www.bdnyc.org/tag/fwhm/` (visited on 02/08/2021).

[35] Bruker BioSpin GmbH. *Bruker homepage on molecular imaging solutions.* URL: `https://www.bruker.com/en/products-and-solutions/preclinical-imaging/nmi/pet-insert.html` (visited on 01/25/2021).

[36] "Bruker BioSpin GmbH". *Performance Evaluation Based on NEMA-NU-2008 In Manufacturing process.* May 2017.

[37] *Micro-PET NEMA-NU4 - Image Quality Mouse Phantom - Datasheet.* URL: `https://www.qrm.de/en/products/micro-pet-iq-phantom/?type=3451&downloadfile=1714&cHash=f710c882edc1614d000079c6837d4539`.

[38] T.H. Farquhar et al. "An investigation of filter choice for filtered back-projection reconstruction in PET". In: *IEEE Transactions on Nuclear Science* 45.3 (June 1998), pp. 1133–1137. DOI: `10.1109/23.681991`.

[39] Peyman Sheikhzadeh et al. “Development and validation of an accurate GATE model for NeuroPET scanner”. In: *Physica Medica* 40 (2017), pp. 59–65. ISSN: 1120-1797. DOI: `https://doi.org/10.1016/j.ejmp.2017.07.008`. URL: `http://www.sciencedirect.com/science/article/pii/S1120179717302259`.

[40] Ville-Veikko Wettenhovi. *OMEGA - Open-source MATLAB Emission Tomography Software*. Sept. 2020. URL: `https://github.com/villekf/OMEGA` (visited on 12/06/2020).

[41] Andreas Markus Loening and Sanjiv Sam Gambhir. “AMIDE: A Free Software Tool for Multimodality Medical Image Analysis”. In: *Molecular Imaging* 2.3 (July 2003), pp. 131–137. DOI: `10.1162/15353500332255687 7`.

[42] Willy Gsell et al. “Characterization of a preclinical PET insert in a 7 Tesla MRI scanner: beyond NEMA testing”. In: *Physics in Medicine and Biology* (June 2020). DOI: `10.1088/1361-6560/aba08c`.

[43] Negar Omidvari et al. “PET performance evaluation of MADPET4: a small animal PET insert for a 7 T MRI scanner”. In: *Physics in Medicine & Biology* 62.22 (Nov. 2017), pp. 8671–8692. DOI: `10.1088/1361-6560/aa910d`.

[44] Laura Moliner et al. “NEMA Performance Evaluation of CareMiBrain dedicated brain PET and Comparison with the whole-body and dedicated brain PET systems”. In: *Scientific Reports* 9.1 (Oct. 2019). DOI: `10.1038/s41598-019-51898-z`.

[45] C.E. Shannon. “Communication in the Presence of Noise”. In: *Proceedings of the IRE* 37.1 (Jan. 1949), pp. 10–21. DOI: `10.1109/jrproc.1949.232969`.

[46] Martin A. Lodge, John J. Sunderland, and Arman Rahmim. “About Measurement of PET Spatial Resolution”. In: *2018 IEEE Nuclear Science Symposium and Medical Imaging Conference Proceedings (NSS/MIC)*. IEEE, Nov. 2018. DOI: `10.1109/nssmic.2018.8824553`.

[47] V.Y. Panin et al. “Fully 3-D PET reconstruction with system matrix derived from point source measurements”. In: *IEEE Transactions on Medical Imaging* 25.7 (July 2006), pp. 907–921. DOI: `10.1109/tmi.2006.876171`.

[48] J. Chaal et al. “A method for estimating PET spatial resolution”. In: *2015 IEEE Nuclear Science Symposium and Medical Imaging Conference (NSS/MIC)*. IEEE, Oct. 2015. DOI: `10.1109/nssmic.2015.7582041`.

[49] Open GATE Collaboration. *GATE documentation*. 2020. URL: `https://opengate.readthedocs.io/en/latest/index.html` (visited on 01/26/2021).

[50] N. Zeraatkar et al. “Accurate Monte Carlo modeling and performance assessment of the X-PET™subsystem of the FLEX Triumph™preclinical PET/CT scanner”. In: *Medical Physics* 38.3 (Feb. 2011), pp. 1217–1225. DOI: `10.1118/1.3547721`.

[51] Krasimir Mitev et al. “Influence of photon energy cuts on PET Monte Carlo simulation results”. In: *Medical Physics* 39.7Part1 (June 2012), pp. 4175–4186. DOI: `10.1118/1.4725168`.

A. Appendix

A.1 Measurement Results

A.1.1 Sensitivity

Position [mm]	**Sensitivity** [cps Bq^{-1}]	**Absolute Sensitivity** [%]	**Position** [mm]	**Sensitivity** [cps Bq^{-1}]	**Absolute Sensitivity** [%]	**Position** [mm]	**Sensitivity** [cps Bq^{-1}]	**Absolute Sensitivity** [%]
-75.20	0.00	0.00	-24.00	0.09	10.24	26.10	0.09	10.20
-74.10	0.01	1.02	-22.00	0.09	10.11	28.00	0.09	9.98
-72.00	0.02	1.69	-20.00	0.09	10.44	30.10	0.09	9.55
-70.00	0.02	2.30	-18.10	0.10	10.79	32.10	0.08	9.20
-68.10	0.03	2.92	-15.90	0.10	11.07	34.00	0.08	8.83
-66.00	0.03	3.70	-14.20	0.10	11.23	36.20	0.08	8.42
-64.00	0.04	4.28	-12.00	0.11	11.66	38.00	0.07	8.06
-62.00	0.04	4.83	-10.10	0.11	11.94	40.10	0.07	7.69
-60.00	0.05	5.55	-8.10	0.11	12.08	42.10	0.07	7.36
-58.00	0.06	6.25	-6.10	0.11	12.32	44.00	0.06	6.87
-56.00	0.06	6.84	-4.10	0.10	11.27	46.10	0.06	6.61
-54.10	0.07	7.43	-2.10	0.10	11.40	48.00	0.07	8.09
-52.00	0.07	7.77	0.00	0.10	11.57	50.20	0.07	7.99
-50.00	0.07	7.99	0.00	0.11	11.67	52.00	0.07	7.84
-48.00	0.07	8.19	2.00	0.11	11.60	54.00	0.07	7.32
-46.00	0.06	6.56	4.10	0.10	11.35	56.00	0.06	6.72
-44.00	0.06	6.93	6.00	0.11	12.53	58.00	0.06	6.08
-42.20	0.07	7.39	8.00	0.11	12.31	60.10	0.05	5.58
-40.00	0.07	7.65	10.20	0.11	12.01	62.00	0.04	4.89
-38.10	0.07	8.06	12.10	0.11	11.77	64.00	0.04	4.26
-36.00	0.08	8.41	14.00	0.10	11.55	66.00	0.03	3.66
-34.00	0.08	8.78	16.00	0.10	11.24	68.00	0.03	3.01
-32.00	0.08	9.18	18.10	0.10	10.92	70.00	0.02	2.40
-30.00	0.09	9.56	20.00	0.10	10.65	71.90	0.02	1.82
-28.10	0.09	9.98	22.00	0.09	10.34	74.30	0.00	0.00
-26.10	0.09	10.22	24.00	0.09	10.19	76.10	0.00	0.00

Table A.1: Measured values for sensitivity measurements